CT Based Lung Cancer Detection Using Spatially Localized Integral Transforms

By

Abel Belay Wossene

In partial fulfillment of the requirement for Degree of Master of Science in Biomedical engineering

Center of Biomedical Engineering
Addis Ababa Institute of Technology
Addis Ababa University

Advisor: Dawit Assefa Haile (PhD)

Addis Ababa, Ethiopia

June, 2018

DECLARATION

I declare that this thesis is my work and that all sources of materials used for this thesis have been properly acknowledged. This thesis has been submitted in partial fulfillment of the requirements for M.Sc. degree in Biomedical Engineering at Addis Ababa University. I earnestly declare that this thesis is not submitted to any other institution anywhere for the award of any academic degree, diploma, or certificate.

Name: Abel Belay Wossene

Signature: _________________

Place: Addis Ababa, Ethiopia

Date of Submission: ______________

This thesis has been submitted for my approval as a university advisor.

Name: Dr. Dawit Assefa Haile

Signature: _________________

Place: Addis Ababa, Ethiopia

Date: ____________________

CT Based Lung Cancer Detection Using Spatially Localized Integral Transforms

By

Abel Belay Wossene

Center of Biomedical Engineering
Addis Ababa Institute of Technology
Addis Ababa University

APPROVED BY BOARD OF EXAMINERS

____________________________	____________________
Chairman, Department of Graduate Committee	Signature
Dr. Dawit Assefa Haile	____________________
Name of Advisor	Signature
____________________________	____________________
Name of External Examiner	Signature
____________________________	____________________
Name of Internal Examiner	Signature

ABSTRACT

Lung cancer is the leading cause of death among other cancer types. Its survival rate is very limited unless diagnosed/detected early. As a result, early detection is imminent for minimizing the deaths caused by lung cancer. For realizing the early detection and early diagnosis, sophisticated and complex imaging modalities like low dose CT are often utilized. However, the big problem lays ahead on the image interpretation. Due to different factors like image quality, suppressed image features in the spatial domain, radiologists eye sight and radiologists' expertise level, misdiagnosis and error are the major difficulties to overcome. In that regard, many research works have been reported in the literature to deal with the image interpretation issues. Among other researches, CADe and CADx are considered the most remarkable methods for early detection and diagnosis. However, most of the CADe and CADx systems are not clinically implemented. This is because of their inefficiency, inaccuracy and non-robustness. Aiming for a more robust and accurate detection of lung cancers, a new computer aided scheme has been suggested in this thesis. The scheme implements a rotation invariant, joint space-frequency localized integral transform together with spatial image enhancement for feature extraction of CT lung images. The algorithm has been implemented on a Matlab platform (Matlab 2013a) and validated on CT lung images acquired from TCIA database. Results showed that the algorithm achieved a sensitivity of 97.1%, specificity of 83.33% and overall accuracy of 96.68% in detecting lung cancers showing its great promise.

Keywords: Lung cancer, CADe, Computed Tomograpghy, Rotation-invariance, Space-Frequency Localized Integral Transform, Feature Extraction, Spatial Image Enhancement.

ACKNOWLEDGEMENT

First of all, I would like to thank the almighty GOD for giving me the strength, patience and guiding me through His never-ending wisdom.

I would like to express my greatest of gratitude to my advisor Dr. Dawit Assefa Haile for his excellent guidance and supervision on the area of my thesis. I couldn’t have done it if it was not for his continuous support and guidance throughout.

Many thanks to the Center of Biomedical Engineering for providing such an opportunity to specialize on this fascinating field of study. I would also want to say thank you to my classmates for sharing their knowledge and being good friends.

Last but not least, I would like to express my greatest and heart felt gratitude to my beloved family; my father Belay, my mother Wubet and my brother Eyob.

TABLE OF CONTENTS

LIST OF FIGURES

LIST OF TABLES

LIST OF ABBREVIATIONS

1D	One Dimension/One Dimesional
2D	Two Dimension/Two Dimensional
4D	Four Dimension/Four Dimensional
CADe	Computer Aided Detection
CADx	Computer Aided Diagnosis
CT	Computed Tomography
CWT	Continuous Wavelet Transform
DICOM	Digital Imaging and Communication in Medicine
FCM	Fuzzy C- means Clustering
FDG	Flouro-deoxy Glucose
FN	False Negative
FP	False Positive
GB	Giga Byte
GHz	Giga Hertz
GLOBOCAN	Global Organization for Cancer
GUI	Graphical User Interface
HSV	Hue-Saturation-Value
Kv	Killo Volt
LDCT	Low Dose Computed Tomography
mA	Milli ampere
Matlab	Matrix Laboratory
mGycm	Milli gray centimeter
mS	Milli sivert
MQU	Mean Quantization Unit
MRI	Magnetic Resonance Imaging
PET	Positron Emission Tomography
RAM	Random Access Memory
ROI	Region of Interest
SMQT	Successive Mean Quantization Transform
STFT	Short Term Fourier Transform
S-transform	Stockwell Transform
TCIA	The Cancer Imaging Archive
TN	True Negative
TP	True Positive
WHO	World Health Organization

CHAPTER 1

INTRODUCTION

1.1 BACKGROUND

Lung cancer is the leading cause of death among other cancer types [1]. According to the estimation by the world health organization (WHO), by the year 2030, lung cancer will be the cause for 17 million deaths worldwide. According to the GLOBOCAN research in 2012, 1.8 million new incidents were reported worldwide, which is 12.6% of all new incidents of all types of cancer in 2012. Studies from the American Cancer Society suggest that, the most common causes of lung cancer are smoking tobacco, second hand smoke, exposure to radon, exposure to asbestos, exposure to diesel exhaust and other environmental factors like breathing polluted air.

Lung cancer is easier to treat at its early stages. It has a survival rate of 47% for early detected lung cancer. However, most lung cancer cases are detected after they are too late to cure. This makes it difficult for the treatment and therapy. In this regard, medical imaging modalities would help a lot in diagnosing lung cancers. Among those modalities chest X-ray is the common one. It is the first test that would be ordered for lung cancer diagnosis. However, chest radiography may be difficult for diagnosis due to failure to detect small peripheral nodules and failure to show cross-sectional view of the lung [2]. For example, findings from the research done by *A. del Ciello et. al* [2] showed that from 82 confirmed cases of lung cancer, 14 of them were missed by the chest radiography. Due to these reasons other modalities are preferred over chest X-ray for better diagnosis.

Other modalities like magnetic resonance imaging (MRI) and positron emission tomography (PET) are also applicable in detection of lung cancers. The MRI with a contrast agent of gadolinium (Gd) and the PET with flouro-deoxy glucose (FDG) are often implemented during diagnosis procedures. However, MRI is often used to find the spread of the cancer to the brain and the PET is nowadays replaced by PET/CT for better cancer detection [3]. PET/CT is a hybrid and costly imaging modality that uses information from both CT and PET [3]. The size of the tumor can be efficiently estimated using CT. PET/MRI is also a hybrid and costly imaging modality that comes with a high contrast resolution but with low detecting power implying high false negatives [3].

CT (Computed Tomography) is another modality used for lung cancer diagnosis. It uses X-rays and is one of the most efficient ways to detect lung lesions [4]. Nowadays, low dose CT scan has shown advancements in lung cancer detection [5]. CT has larger radiation in milli-seivert (mS) as compared to chest X-ray. However, low dose CT with 25 milli-ampere (mA)/80 kilo-volt (kv) and radiation dose of 22.3 milli-gray centimeter (mGycm) (approximately 0.3mS) does not affect the sensitivity for the lung cancer [6]. The radiation dose of the low dose CT (LDCT) which is 0.3-0.6mS is very small as compared to the 3.5-7mS of normal CT [5] [6]. Small nodules are never missed in CT. Figure 1.1 shows CT images of a normal as well as a patient with confirmed lung cancer.

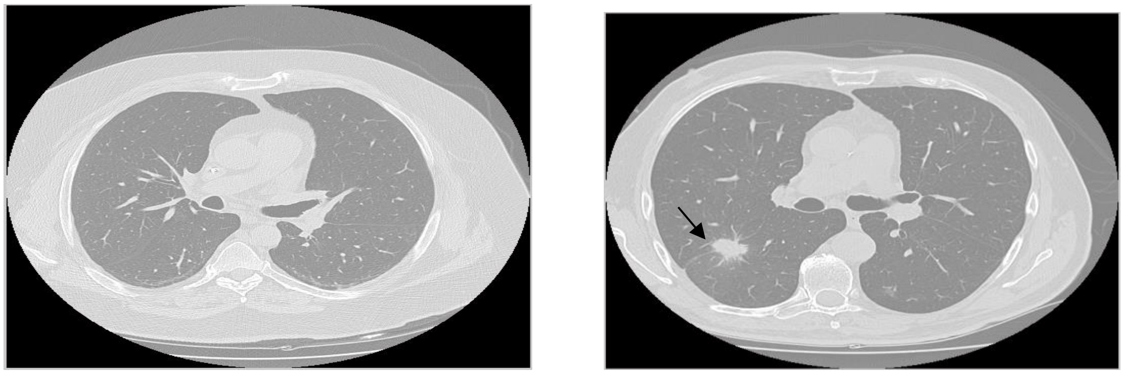

Figure 1.1: CT image with lung cancer (Right) and another without lung cancer (Left).

Eventhough CT is very sensitive, it comes with difficulties when trying to visually differentiate between benigness and malignancy [7]. As a result, high false positive is always the problem to overcome. This calls for the development of a CADe (Computer Aided Detection) system. CADe and computer aided diagnosis (CADx) are considered the two very remarkable ways for early detection of lung cancers [1].

CADx characterizes and measures the lesion in addition to lesion detection. It also stages the cancer level [7]. On the other hand, in CADe the original image will be input to the system and the enhanced region of interest (ROI) will be the output of the system. The output is very helpful for decision making [1] [7]. This will enhance the quality of the medical service through improving the diagnosis accuracy and assists in the early detection of the cancer. According to the study by *K. N. Jeon et al.,* CADe increases the efficiency of radiologists in nodule detection [8]. In an experiment conducted in 2012 on 132 CT images of the lung, it was observed that the radiologists' efficiency was improved from 77% to 84% when they used the CADe system [8]. Most of the CADe systems, however, are not implemented clinically. This is because of the inaccuracy and inefficiency of the image segmentation algorithms of the CADe [7]. There is still a call for the development of a robust and more accurate segmentation algorithm.

Most CADe systems have similar stages; signal acquisition, preprocessing, segmentation and detection [7]. This is so for most methods implemented both in spatial domain and also on a transformed domain (eg. frequency domain). In the latter case, different integral transforms are used including the 2D Fourier transform, 2D Hartley transform and the like. Image processing in the spatial-frequency (wave number) domain has its own advantages for fast computation, alternative representation and sensing and better image processing [9]. It is very best for image denoising through periodic filters [10]. The 2D Fourier transform is one such transform that has been used in many different applications in imaging and image processing. Hartely transform is the same as Fourier transform but it computes the coefficients of the Fourier transform in the real space without involving complex arithmetic [11]. Such transforms are known to be adequate for analyzing 2D images (signals) which are stationary in that the images' frequency characteristics does not change spatially. However, most medical images show spatial frequency variation. In that regard, joint space-wave number (spatial frequency) transforms are already available for a better localized analysis of 2D images [10]. These include the 2D Gabor transform and the 2D wavelet transform.

Filtering of an image could be done in spatial-frequency transformed domain. For example, a log Gabor filtering was used on *M.V. Ajil et al.* for image preprocessing on CT images due to its reduced DC value and extendedness at high frequency [12]. In some occasions 2D Gabor transform can be used for feature extraction. Using filter banks of different emphasis, features of an image can be extracted [13]. Thus, Gabor filtering is applied in many image enhancements. However, Gabor transform uses a fixed sliding window. This makes it challenging to track ever changing frequencies in an image and for image feature extraction in the Gabor transform [14].

Wavelet domain noise removal is also possible. The 2D wavelet transform is a spatially localized transform like the Gabor transform but applies multi-resolution analysis as opposed to the fixed localizing window used in Gabor filters [10-14]. On a previous research made by *L. Gabralla et al.* [15], images were first transformed into component wavelets. After that a filter with a threshold calculated by: $T_{new} = \sigma' \sqrt{2\log(n) - 8\left(\frac{\sigma 1(x)}{\mu(x)}\right)}$ is applied and then filtered images were reconstructed (where $\boldsymbol{n}$ is the sample size, $\boldsymbol{\sigma'}$ is an estimate of the noise level, while $\boldsymbol{\sigma 1}$ and $\boldsymbol{\mu}$ are respectively the variance and the mean of the input noisy image) [15]. This technique was proven to be good to deal with Gaussian and speckle kinds of noises [15].

Wavelet domain image enhancement could also be used for image segmentation and enhancement. In *I. Khalifa et al.* the discrete 2D wavelet transform was used to segment MRI brain images using 4 different filter banks, the low pass, high pass horizontal, high pass vertical, and high pass diagonal [16]. Then using those output images, clustering and segmentation of the original image was carried out using FCM (fuzzy C-means clustering).

The Stockwell (S) transform is another way to process an image in spatial-frequency domain [17] [18]. The S-transform is mainly a phase correction of the wavelet transform [17]. The S-transform keeps the Absolutely referenced phase information while the wavelet transform does not. Compared to wavelets, the S-transform does have a more direct relation with the natural complex Fourier transform which makes it easier to implement and calculate its inverse [17].

The 2D extension of the S-transform is quite similar [18]. In *D. Assefa et al*. the rotation invariant 2D S-transform was proposed for use in texture analysis of color images extending the definition to the quaternion space [19]. S-transform is easily invertible with explicit relation with the Fourier transform while invertibility of the wavelet transform depends on the choice of the mother wavelet as well as the so-called admissibility criteria. The S-transform has better frequency resolution for wider spatial domain window at lower frequencies and better time resolution at higher frequencies [17]. The S transform has been used in different filtering and other image processing applications.

In this thesis the rotation invariant 2D S-transform has been applied to design the lung cancer image feature extraction scheme. Its typical advantages in-terms of simplicity and other important properties of interest is demonstrated and an algorithm is developed based on the rotation invriant 2D S-transform for use in effective segmentation of malignant lung nodules.

Several image-processing tools for tumor detection schemes are reviewed in this thesis discussing their merits and demerits and a new method has been proopsoed. Thoracic images of lung cancer patients acquired on a low dose CT scanner are used to test the efficacy of the proposed method. Manual delineations drawn by expert physicians and radiologists are used as gold standards/ground truth. The images with their gold standards were acquired from the cancer imaging archive (TCIA).

1.2 PROBLEM STATEMENT

Lung cancer being the leading killer of all cancer types, its early detection is of imminent advantage in reducing the death rate. For realizing the early detection and early diagnosis, sophisticated and complex imaging modalities like low dose CT are often utilized. However, there is a high risk of misdiagnosis and error in interpretation of lung CT images at early stages inside the clinics. Many researches on CADe have been carried out in the literature to reduce the risk of error and misdiagnosis. In this regard, methods based on integral transforms have shown great promises. The current work intends to show a new method for lung tumor detection on CT images based on an integral transform that is simple and has useful properties which are relevant during development of an efficient detection scheme.

1.3 OBJECTIVES

1.3.1 GENERAL OBJECTIVE

The main objective of this thesis is to design an integral transform based, robust and efficient image segmentation and feature extraction algorithm for computer aided lung cancer detection (CADe) based on CT images captured on a low dose CT scanner.

1.3.2 SPECIFIC OBJECTIVES

- Discuss the usefulness of an integral transform that is a simple extension of the natural Fourier transform and its important properties for use in effective image processing.
- Develop an integral transform-based lung cancer detection scheme by computing useful features (textures, patterns) from CT images in the transformed domain.
- Test the accuracy and robustness of the method through qualitative and quantitative evaluation techniques against available gold standards (ground truth).
- Investigate possible clinical implications of the method.

1.4 SIGNIFICANCE OF THE THESIS STUDY

Undoubtedly better diagnosis brings better medical care. The cancer detection algorithm developed in this thesis has been validated on low dose CT images acquired from a research database and it resulted in an accurate and efficient lung cancer detection outcome. Accuracy and efficiency lead to better diagnosis and detection by reducing the cost of diagnosis. As a result, it helps in bettering the healthcare service as a whole by reducing the death rate caused by lung cancer. It also could bring ease of diagnosis and will be interoperable with the present day electronic medical records and electronic health recording systems in general. The biggest problem is not in getting access to the medical device, rather it is in getting the service. For better service, available expert radiologists have to be used efficiently and the development of such an automated detection system means that much of their time spent on staring on images would be reduced to a minimum. This creates way for quicker diagnosis and efficient usage of radiologists through application of tele-medicine.

1.5 SCOPE AND DELIMITATION OF THE THESIS

This thesis has been validated on a Matlab 2013a platform. Test images were acquired from the TCIA (The Cancer Imaging Archive) database and some low-resolution images snapped from publications were also considered (to test the robustness at low resolution and contrast). The algorithm was not implemented clinically which limits the testing step only to the images from the database and the snapped images.

In the algorithm, much attention was given to the feature extraction and detection of abnormal nodules and differentiation of normal nodules from abnormal ones located inside the lung parenchyma. The lung images from the downloaded database were used depending on their response to marker-controlled watershed transform to segment only the lung part. The tests are not made on images with cancer tumors located on the edges of lung parts due to their response to the marker-controlled watershed transform.

1.6 ORGANIZATION OF THE THESIS

The rest of the thesis has been organized into five chapters. Chapter 2 gives an explanation and in-depth literature on different integral transforms. Since the thesis used an integral transform method for feature extraction, the chapter also provides a summary on the advantages and disadvantages of each integral transform with literatures to support the premises. Chapter 3 is about spatial image enhancement techniques. It explains and discusses the advantages and disadvantages of spatial enhancement techniques that have been mentioned/implemented on the later parts of the thesis.

Chapter 4 shows the detailed stages and procedures that have been implemented in the thesis. It shows what method has been used in each stage of the procedure and explains the reasons in details. It also explains what materials were used and implemented so as to test the developed algorithm. Chapter 5 explains the results and what they meant. Demonstrating results are presented and discussed. Chapter 6 presents conclusions and possible future works.

CHAPTER 2

INTEGRAL TRANSFORMS

2.1 THE FOURIER TRANSFORM

The concepts of Fourier series and Fourier transform were raised by the French Mathematician Jean Baptiste Joseph Fourier on his published book in 1807 [9]. The concept of Fourier series is a representation of any periodic function which satisfies the piecewise linearity as the sum of sines and cosines with their respective coefficients [9]. On the other hand, Fourier transform is the sine and cosine integral representation of a function [9]. The complex Fourier transform contains two components, the phase and amplitude (magnitude) [20]. It gives ways to measure and find out the frequency contents of a signal (a time series in 1D and image in 2D) [14]. The Fourier transform is lossless transform in the sense that a signal could be completely recovered from its Fourier transform using the inverse Fourier transform [9]. In Fourier transform the phase gives the information about the angle shift which would be useful in inverse transformation of the signal back to spatial domain [20].

Even though the Fourier transform was first proposed for solving heat diffusion, it also played great roles in different aspects of signal and image processing [9]. The introduction of the Fast Fourier Transform (FFT) in 1960s provided even a great opportunity for faster analysis of signals [9].

For a given periodic signal *f(t),* its Fourier series and the respective Fourier coefficients *Cn* can be computed as:

$$f(t) = \sum_{n=-\infty}^{\infty} Cn\ exp^{\frac{j2\pi nt}{T}} \qquad (2.1)$$

$$Cn = \frac{1}{T}\int_{-T/2}^{T/2} f(t) exp^{-j2\pi nt/T}\, dt \qquad (2.2)$$

Similarly, the 1D continuous Fourier transform of *f(t)* and its inverse can be computed as:

$$F(\omega) = \int_{-\infty}^{\infty} f(t) exp^{-j2\pi\omega t}\, dt \tag{2.3}$$

$$f(t) = \int_{-\infty}^{\infty} F(\omega) exp^{j2\pi\omega t}\, d\omega \tag{2.4}$$

where t is time, ω is frequency and $j = \sqrt{-1}$. The discrete version of the 1D Fourier transform of a sequence of length *M* and its inverse are given by:

$$F(m) = \sum_{n=0}^{M-1} f(n) exp^{\frac{-j2\pi nm}{M}} \qquad m = 0, 1, 2, \ldots, M\text{-}1 \tag{2.5}$$

$$f(n) = \frac{1}{M}\sum_{n=0}^{M-1} F(m) exp^{\frac{j2\pi nm}{M}} \qquad n = 0, 1, 2, \ldots, M\text{-}1. \tag{2.6}$$

where *n* represents the discrete time and *m* represents discrete frequency variables.

The 2D Fourier transform is often applied to analyze 2D signals (images) and transforms the signals from the spatial domain to the respective spatial frequency (wave-number) domains. The discrete version of the 2D Fourier transform and its inverse are computed using the Eq. 2.7 and Eq. 2.8. There is a 2D version of the FFT that is used to compute the 2D Fourier transform efficiently. *M* and *N* are the lengths of the sequence in the *x* and *y* directions.

$$F(u, v) = \sum_{x=0}^{M-1} \sum_{y=0}^{N-1} f(x, y)\, exp^{-j2\pi(\frac{ux}{M} + \frac{vy}{N})} \tag{2.7}$$

$$f(x, y) = \frac{1}{NM}\sum_{u=0}^{M-1} \sum_{v=0}^{N-1} F(u, v)\, exp^{j2\pi(\frac{ux}{M} + \frac{vy}{N})} \tag{2.8}$$

where *x* and *y* represents the discrete space and *u* and *v* represents discrete frequency.

The 2D Fourier transform has many interesting properties: it is linear and rotation invariant. Convolution in the spatial domain is the same as product in the Fourier domain as shown in Eq. 2.9 below.

$$f(x, y) * h(x, y) \rightarrow F(u, v)H(u, v) \tag{2.9}$$

where *F* and *H* are the Fourier transforms of *f* and *h* respectively.

The basic principle of the Fourier transform is frequency representation of a signal be it 1D or 2D. Sometimes the information about the signal may not be straight forward and thus would be difficult to obtain valuable information in the time/space domain [14]. Much of the details may be encrypted in the frequency of the signal. Operations such as convolution/filtering are much easier in the frequency domain than the original time/space domain. This is because in the Fourier domain convolution is straight multiplication which led it to be the usual implementation of many filters like butter worth, gaussian, notch, bandpass and band stop in frequency domain [9].

In image processing, Fourier transform has a great deal of advantages. Frequency based approaches provide better image processing, faster computation, alternative representation and sensing, as well as efficient storage [9]. Sometimes images could be acquired under low illumination. This may create unevenness in the image brightness. Also due to imperfectness of the image acquisition techniques, images could appear blurry and noisy. As a result, images may not have sufficient spatial resolution. Thus, it is reasonable to use frequency domain image processing techniques to overcome these issues [21] [22]. Eventhough, Fourier domain signal processing is advantageous, it does have some drawbacks when applied on non-stationary signals for processing [10]. The Fourier transform only assumes the signal to be stationary and represents the transformed signal exhibiting peaks at representative frequencies without any regard to their spatial locations [10].

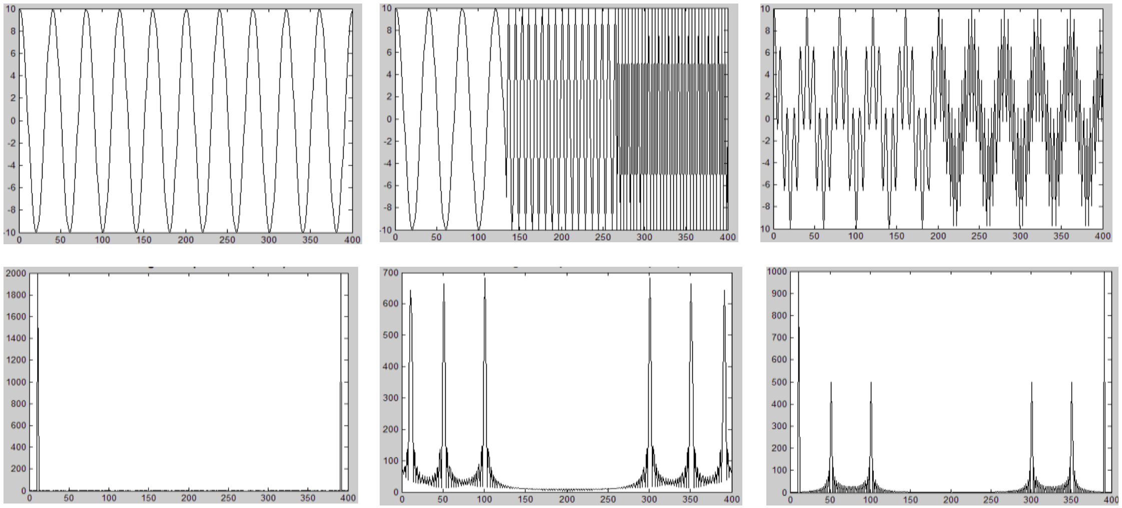

FIGURE 2.1: THE 1D FOURIER TRANSFORM OF DIFFERENT SIGNALS. A B C
D E F

(A) *$f(x) = 10cos(20\pi \frac{x}{N})$, $x \in$ [0:N] with only a single frequency (stationary signal),* ***(B)*** *$f(x) = 10cos(20\pi \frac{x}{N})$, $x \in$ [0:N/3], $f(x) = 10cos(100\pi \frac{x}{N})$, $x \in$ [N/3+1:2N/3], $f(x) = 10cos(200\pi \frac{x}{N})$ $x \in$ [2N/3+1:N], three consecutive frequencies ,* ***(C)*** *$f(x) = 5cos\left(20\pi \frac{x}{N}\right) + 5cos(100\pi \frac{x}{N})$, $x \in$ [0:N/2], $f(x) = 5cos\left(20\pi \frac{x}{N}\right) + 5cos(200\pi \frac{x}{N})$, $x \in$ [N/2+1:N], three frequencies but one frequency component exists at all times where N is the number of sample points. .* ***(D)****,* ***(E)****, and* ***(F)*** *represent the respective Fourier amplitude spectra.*

This implies that Fourier domain filters are very successful in attenuating additive and periodic noise. However, real images, especially medical images, are known for their non-stationary nature and randomness of their noise distribution [14]. Figure 2.1 presents three 1D signals: the first one was a stationary signal with a 10 Hz frequency, the next one was a non-stationary signal with three frequency components one after the other. The last signal is again non-stationary but is composed of a frequency component that exists all the time and two other frequency components in two different intervals. The Fourier amplitude spectra for the later two signals appeared somehow similar (each showed six picks including the symmetry) despite the two signals are completely different and their frequency components are found at different locations. The same issue exists when analyzing 2D images using the 2D Fourier transform. For that reason, it is often difficult to extract useful image features only from its Fourier amplitude or phase spectra [14]. Transforms that offer spatially localized frequency information should present a better alternative when analyzing such signals with spatially/temporally dependent frequency characteristics.

2.2 THE GABOR TRANSFORM

The Gabor transform was first introduced by the Danish mathematician Denis Gabor in 1946 on his published article "*Theory and communication*" [23]. The idea was to make the 1D Fourier transform temporally localized [23]. The Gabor transform also called the Short-term Fourier transform (STFT) is applied to signals to study the localized frequency representation [14].

The continuous Gabor transform is a simple localization of the Fourier transform through a sliding window [14]. The translation and the frequency value are the two variables that are involved in the 1D Gabor transform given by [10] [14].

$$G(b,\omega) = \int_{-\infty}^{\infty} f(t)g\,(t-b)exp^{-j2\pi\omega t}dt \tag{2.10}$$

$$g(t) = \frac{1}{\sqrt{2\pi}\sigma} exp^{-\frac{1}{2}(t^2/\sigma^2)} \tag{2.11}$$

where f is the input signal, G is the Gabor transform which is a function of the translation variable b (essentially a time variable) and frequency variable ω, while g is the localizing window function (the normalized Gaussian with *width* σ). The 2D Gabor transform is defined in a similar way as a function of two translation variables (essentially spatial variables) and two spatial-frequencies (wave-numbers) in the x and y directions respectively and is given by:

$$G(\tau_{x,}\tau_{y,}\omega_{x,}\omega_{y,}) = \iint_{-\infty}^{\infty} f(x,y)g(x-\tau_{x,}y-\tau_y)exp^{-j2\pi(x\omega_x+y\omega_y)}dxdy \tag{2.12}$$

The discrete version of the 2D Gabor transform is given by:

$$G(k,l,u,v) = \sum_x \sum_y f(x,y)g(x-k,y-l)exp^{-j2\pi(\frac{ux}{M}+\frac{vy}{N})} \tag{2.13}$$

for $k, u = 0, 1, \ldots, M-1$; $l, v = 0, 1, \ldots, N-1$; M, N are the lengths in x and y directions respectively for an input 2D discrete signal $f(x,y)$.

The localizing window is permitted to translate in both x and y directions and that way all image pixles will be traced and the end result is a joint space frequency information available for further image processing.

The discrete version of the 2D Gabor transform is mostly used for image feature extraction and denoising applications. For example, in a previous study Gabor filtering was used for feature extraction of images using filter banks with different orientations [13]. Figure 2.2 presents Gabor filter banks with different orientations.

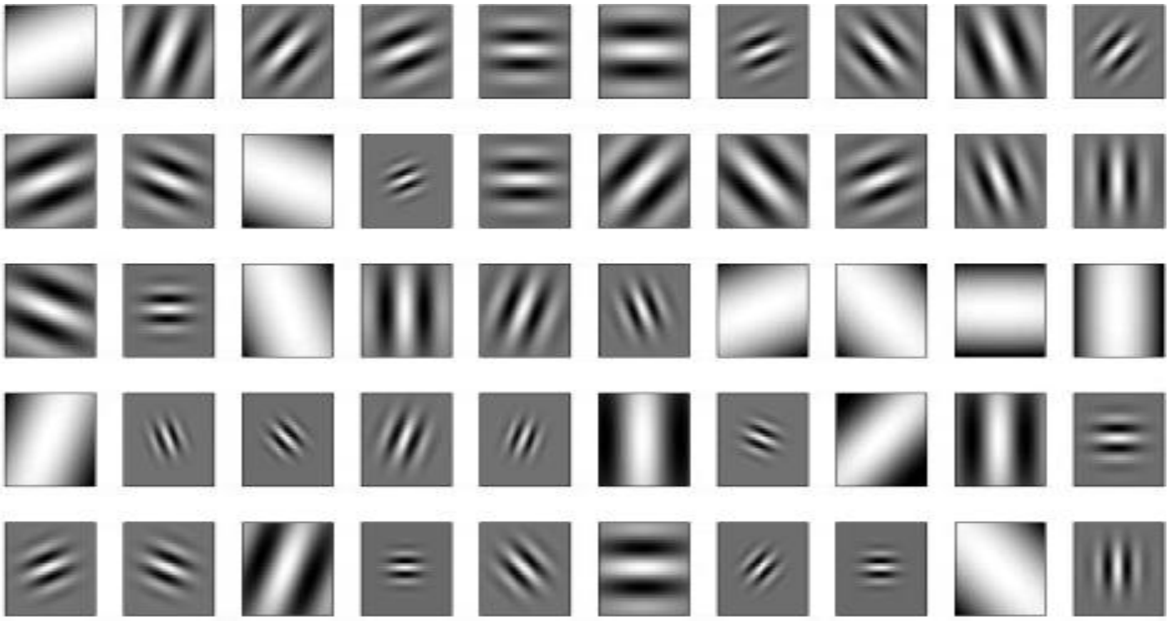

FIGURE 2.2: GABOR FILTER BANKS WITH DIFFERENT ORIENTATIONS:
The 50 Gabor wavelet filters were chosen by a selection algorithm for use in breast tissue classification based on mammograms (Images acquired: http://www.biomedical-engineering-online.com/content/10/1/55).

One major drawback with the Gabor transform is that the localizing window size is never changing. Once we choose a window size, it will be used throughout the signal. If wider window is chosen, then the spatial resolution will be degraded whereas the frequency resolution will be enhanced. On the other hand, if we use a narrower window, spatially the signal will be resolved whereas the frequency resolution will be degraded. This is because of Heisenberg's uncertainty principle. It states that it is impossible to represent signals time-frequency representation with perfect resolution for both frequency and time (space in images) [10]. This makes it difficult to choose the optimal window size for the whole signal, especially for medical images with non-stationary frequency characteristics.

2.3 THE WAVELET TRANSFORM

In 1982 the French geophysicist Jean Morlet introduced the concept of wavelets [24]. Wavelet means a small wave: the smallness refers to the condition that the wavelet function (window function) is of finite length (compactly supported) while the wave refers to the fact that the function is oscillatory [14] [24] [10]. The idea of wavelet transform was primarily intended to study seismic signals [24]. Late Alex Grossman studied the inverse of the wavelets. The two scientists jointly came up with study of continuous wavelet transform [24]. The wavelet transform is applied to signals for localized frequency processing [14].

The 1D continuous and discrete forms of the wavelet transform are given by equations 2.14 and 2.15 respectively.

$$W\psi(s,\tau) = \frac{1}{\sqrt{s}}\int_{-\infty}^{\infty} f(x)\psi(\frac{x}{s} - \frac{\tau}{s})dx \tag{2.14}$$

$$W\psi(j,k) = \frac{1}{\sqrt{M}}\sum_n f(n)\psi_{j,k}(n) \tag{2.15}$$

where f is the 1D signal, ψ represents the mother wavelet, τ is the spatial translation and s represents the scaling parameter (dilation parameter).

The 2D wavelet transform is similarly defined in 2-space as:

$$W\psi(s,\tau,u,v) = \frac{1}{\sqrt{s(x,y)}}\iint f(x,y)\,\psi_{s(x,y)}^{\tau(x,y)}(k-x,l-y)dxdy \tag{2.16}$$

The translation variable dictates the location of the window while the scaling parameter dictates its size. The scale is the same as its concept in maps; high scale means non-detailed or general information, whereas small scale is detailed information [14].

Naturally images contain most of the energy concentrated in the low frequency. Therefore, it is possible to extract the image information to some content by decomposing the spatial frequency spectrum [25]. The basic concept of the wavelet transform is to give better frequency resolution for lower frequencies and better spatial resolution for higher frequencies [14]. As a result, it gives variable window size for different frequencies instead of having a fixed window as in the Gabor transform [14]. That is basically the concept behind multi-resolution signal analysis.

In wavelet transform first the mother wavelet must be selected. Then the computation starts by setting the value of the scale ***s*** to 1. Then, for continuous wavelet transform, Equation 2.14 will be evaluated for all values of ***s***. However, since most of the signals are bandlimited, it is not necessary to compute the result for all values of ***s***. Therefore, the analysis starts at ***s = 1*** and continues for greater values of ***s***. In other words, the analysis starts at higher frequencies and continues for low frequencies [14]. After evaluating the transform for all values of ***s***, the signal shifts by the window size and the calculation continues for the second phase again [14] [10]. Eventhough, it is impossible to avoid the Heisenberg's uncertainty, this way the frequency-time resolution is better. There are different wavelets to choose from and Figure 2.3 presents some of them.

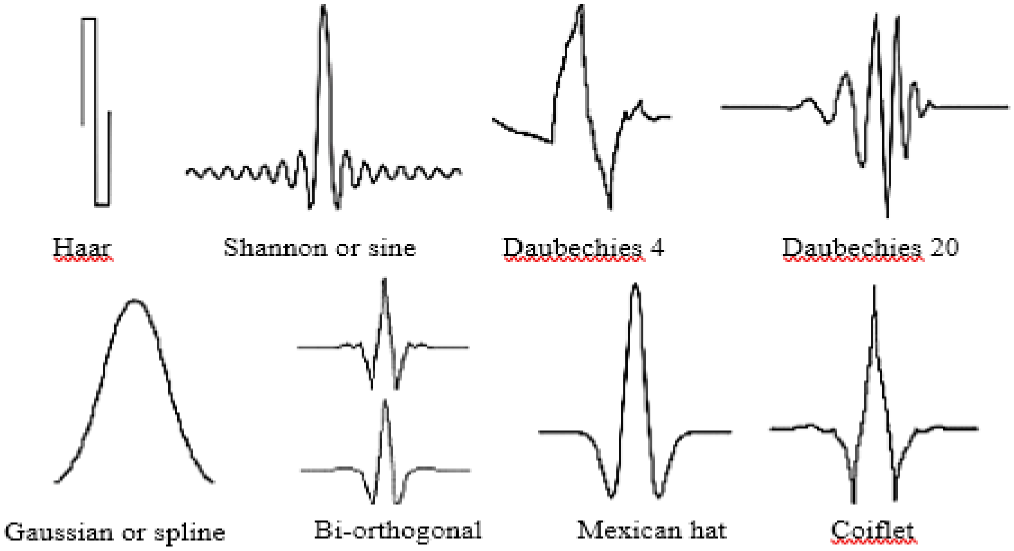

FIGURE 2.3: EXAMPLES OF WAVELET:
(Images acquired: http://antiege.org/best-forex-trading-app/forex-wavelet-trading-php).

Wavelet transform possess better frequency resolution for wider window size and better spatial resolution for narrow window sizes. There are two basic differences between Gabor and the wavelet transform:

- In wavelets, there is no Fourier transform implementation resulting in negative frequencies;
- The width of the window in wavelet transform is variable (dependent on the frequency of the signal) which paves a way for better resolution [14].

Discrete wavelet transform is easier to implement, it contains the concept of sub-sampling [14]. First the signal with a certain sequence size will be inputted to the system. Then the signal will be filtered by set of high pass filters and low pass filters. This gives out an output of two frequency bands, the high frequency and low frequency bands. In the process every other signal sequence is dropped if the scale $s = 2$. Then the low passed signal will again be filtered by high pass and low pass filters. Through this iteration the signal may lose its details and resolutions yielding multiple resolution signals at every step on the way. Figure 2.4 below shows the process involved in the fast wavelet transform implementation.

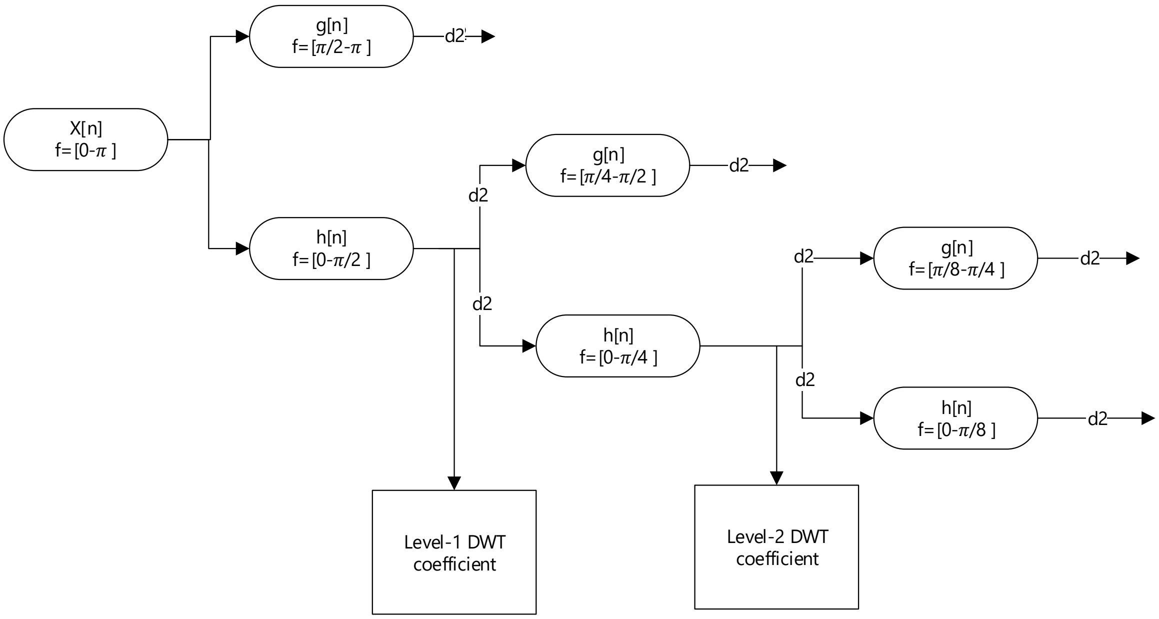

FIGURE 2.4: SCHEMATIC OF THE FAST WAVELET TRANSFORM ALGORITHM.

The same procedures are applied for 2D discrete signals. There are concepts called image pyramid and sub-band which are basically the collection of images with decreasing resolution [9]. Subsampling (down sampling) drops samples. For example, in Figure 2.4 above, the down sampling denoted by **d2** represents that every other signal is going to be dropped in each step of filtering. The filters are denoted by **h[n]** and **g[n]** which are low pass filter and high pass filters respectively.

One issue with the wavelet transform is that invertibility of the wavelet transform depends on the choice of the mother wavelet as well as the so-called admissibility criteria [17]. Moreover, the discrete wavelet transform is computationally less efficient and more difficult to interpret since it has no direct relation with the natural Fourier transform. In addition to that, the transform by itself introduces some noise to the signal which poses the treat of choosing a wavelet for specific application [17].

2.4 THE STOCKWELL (S) TRANSFORM

The S-transform, which was introduced in 1996 by R. G. Stockwell, is another spatial-frequency representation of a signal. It was an extension to the continuous wavelet transform (CWT) and is based on a moving and scalable localizing gaussian window. S-transform possesses some desirable characteristics that wavelet or any other transforms don’t possess [17] [18].

The S-transform is unique in that it provides frequency-dependent resolution while maintaining a direct relationship with the natural complex Fourier transform [17]. These advantages of the S-transform are due to the fact that the modulating sinusoids are fixed with respect to the time axis, whereas the localizing scalable Gaussian window dilates and translates.

From Equation 2.14 in the wavelet transform definition, we know that $\boldsymbol{\tau}$ represents the time translation of the signal. Thus, the S-transform of a 1D function *f(t)* is defined as a continuous wavelet transform with a specific mother wavelet multiplied by the phase factor. This gives rise to Equation 2.17 with the *window function* defined in Equation 2.18. The window function used in the S transform is actually the normalized Gaussian whose width is set to be inversely related to the frequency.

$$S(\tau, \omega) = exp^{j2\pi\omega t\tau}\ w(\tau, d) \tag{2.17}$$

$$w(t, \omega) = \frac{|\omega|}{\sqrt{2\pi}} exp^{-\frac{(\tau-t)^2\omega^2}{2}} \tag{2.18}$$

The S-transform can be written explicitly as in Equation 2.19. As seen in Equation 2.20, the integral of the S-transform with respect to the translation variable is nothing but the complex Fourier transform of the input signal showing the direct relationship that exists between the S-transform and the Fourier transform.

$$S(\tau, \omega) = \int_{-\infty}^{\infty} f(t) \frac{|\omega|}{\sqrt{2\pi}} exp^{-\frac{(\tau-t)^2\omega^2}{2}}\ exp^{-j2\pi\omega t} dt \tag{2.19}$$

$$\int_{-\infty}^{\infty} S(\tau, \omega)\, d\tau = F(\omega) \tag{2.20}$$

Using the convolution theorem, the discrete form of the S-transform is explicitly given by:

$$S\left[iT, \frac{n}{NT}\right] = \sum_{m=0}^{N-1} H\left(\frac{m+n}{NT}\right) exp^{\frac{-2\pi^2 m^2}{n^2}} exp^{\frac{-j2\pi mi}{N}} \tag{2.21}$$

where $n \neq 0, \omega \rightarrow \frac{n}{NT}, \ \tau \ \rightarrow iT$, T is the time step and

$$H\left[\frac{n}{NT}\right] = \frac{1}{N} \sum_{k=0}^{N-1} f(kT) exp^{-\frac{j2\pi kn}{N}}, \qquad n = 0, 1, 2, \ldots, N-1, j = \sqrt{-1}.$$

The continuous 2D S-transform is similarly defined and is given in Equation 2.22.

$$S(X, Y, \omega_x, \omega_y) = \iint f(x, y) \frac{|\omega_x \omega_y|}{\sqrt{2\pi k_1 k_2}} exp^{\frac{-(\tau_x - X)^2 \omega_x^2}{2k_1^2} - \frac{(\tau_y - Y)^2 \omega_y^2}{2k_2^2}} exp^{-j2\pi(x\omega_x + y\omega_y)} dxdy$$

(2.22)

where $k_1 = \delta_x |\omega_x|$, $k_2 = \delta_y |\omega_y|$, $\delta_x \ and \ \delta_y$ are the 2D Gaussian window widths, $\tau_x \ and \ \tau_y$ are the translation variables while ω_x and ω_y are the spatial-frequencies (wave-numbers) in x and y directions respectively. Note that $k_1 \ and \ k_2$ are the constants of proportionality between the Gaussian width and the spatial-frequencies in the respective directions and they both dictate the slope of the Gaussian.

Figure 2.5 and Figure 2.6 present comparisons between the natural Complex Fourier transform, the Gabor transform, the wavelet transform and the S transform considering two 1D signals: one stationary while the other non-stationary. The Fourier transform offers perfect frequency resolution and is adequate for the stationary signal but failed to offer adequate information when applied on the non-stationary signal as it completely misses the temporal information. The Gabor transform (with 8 segments width window) suffers from the fixed resolution issues while the wavelet transform appeared to be quite noisy. The performance of the S transform was quite commendable in both cases with a reasonable resolution of both the time and frequency components of both signals with minimal noise. There is however, one issue with the 2D S transform as it is defined earlier in Equation 2.22 was its rotation variant nature. The issue has been resolved in a study done by *D. Assefa et al.* [19] in their study to use the transform for novel color texture analysis and patter recognition by extending the concept from the complex 2D space to the quaternion 4D space [19].

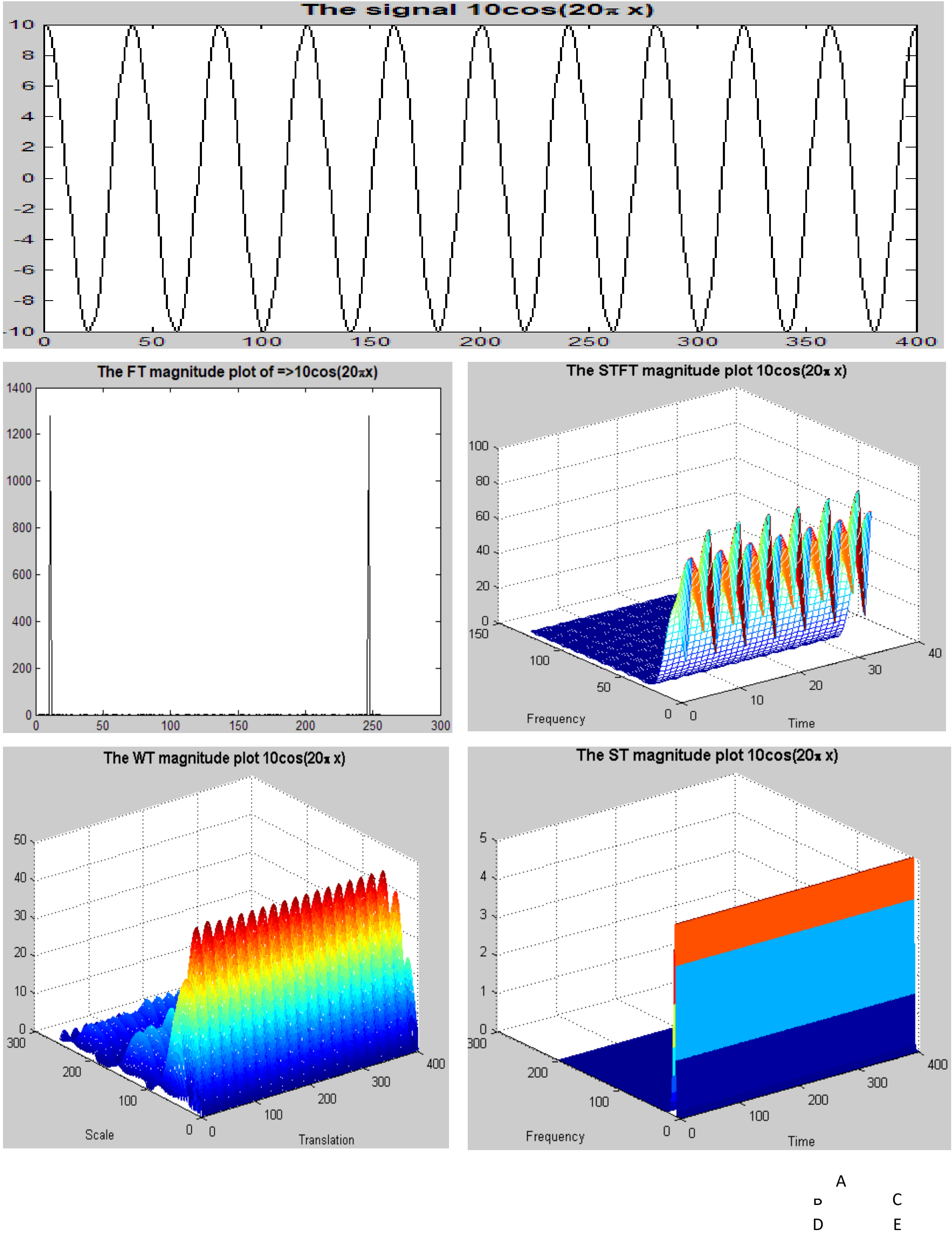

*FIGURE 2.5: IMPLEMENTATION OF THE FOURIER (**B**), GABOR (**C**), WAVELET (**D**)AND S TRANSFORMS (**E**)FOR A STATIONARY SIGNAL (**A**).*

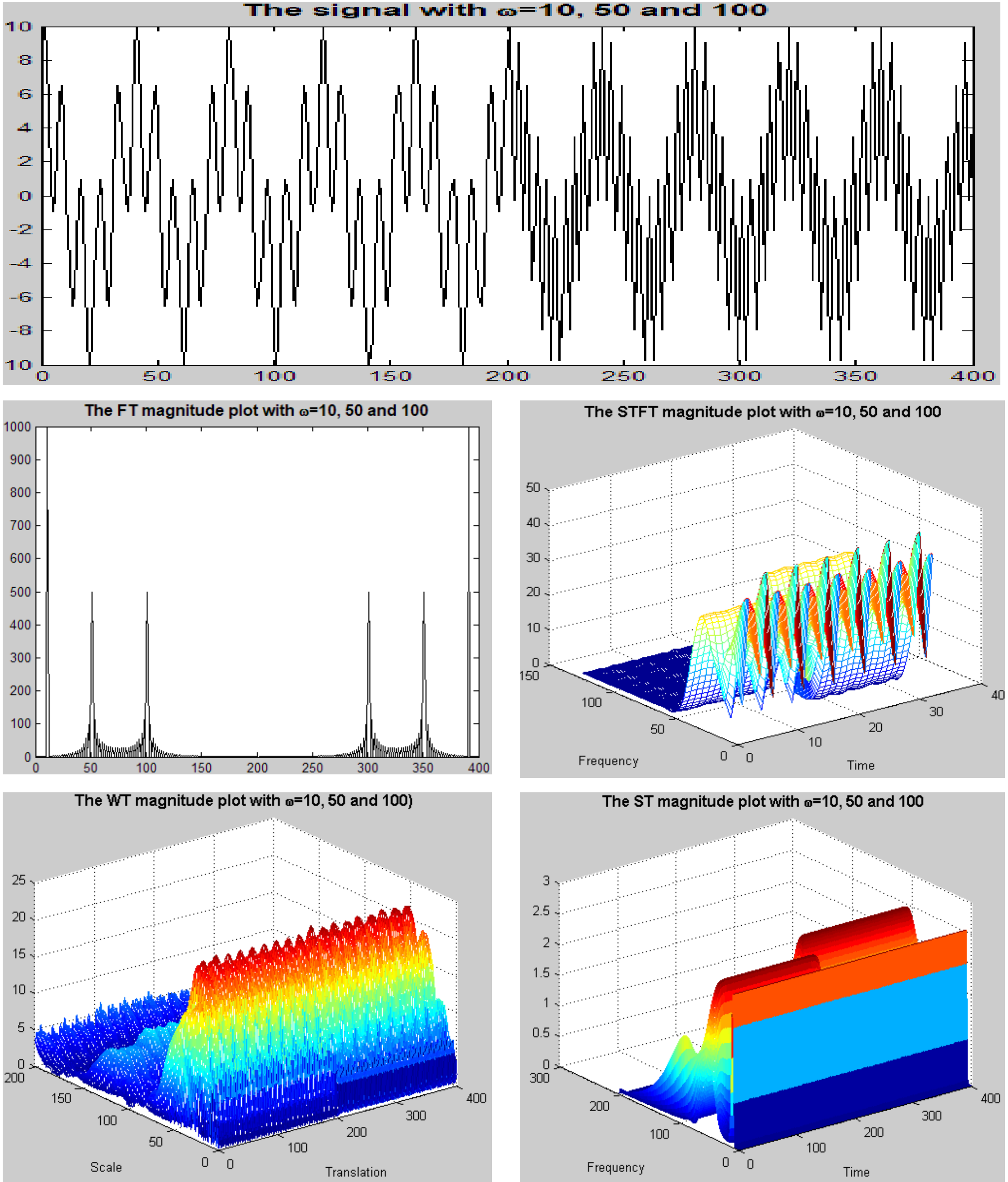
The signal with ω=10, 50 and 100

The FT magnitude plot with ω=10, 50 and 100

The STFT magnitude plot with ω=10, 50 and 100

The WT magnitude plot with ω=10, 50 and 100)

The ST magnitude plot with ω=10, 50 and 100

*Figure 2.6: Implementation of the Fourier (**b**), Gabor (**c**), Wavelet (**d**)and S (**e**) transforms for a non-stationary signal (**a**).*

A
B C
D E

The rotation invariant 2D S transform is given by [19]:

$$S\left(X,Y,\omega_x,\omega_y\right)=\iint f(x,y)\,\frac{\omega_x^2+\omega_y^2}{2\pi r^2}\,exp^{-\{(\tau_x-X)^2+\left(\tau_y-Y\right)^2\}\frac{(\omega_x^2+\omega_y^2)}{2r^2}}\,exp^{-j2\pi\left(x\omega_x+y\omega_y\right)}dxdy$$

(2.23)

where, $\delta=|r|\sqrt{\omega_x^2+\omega_y^2}$ *is* the variable 2D Gaussian width and r is a constant that dictates the slope of the 2D Gaussian localizing window. The two images in Figure 2.7 demonstrate the differences between the rotation invariant (with circular cross-section) and the non-rotation invariant (with elliptic cross-section) 2D Gaussian windows. More discussion on the issue is available on the original paper [19].

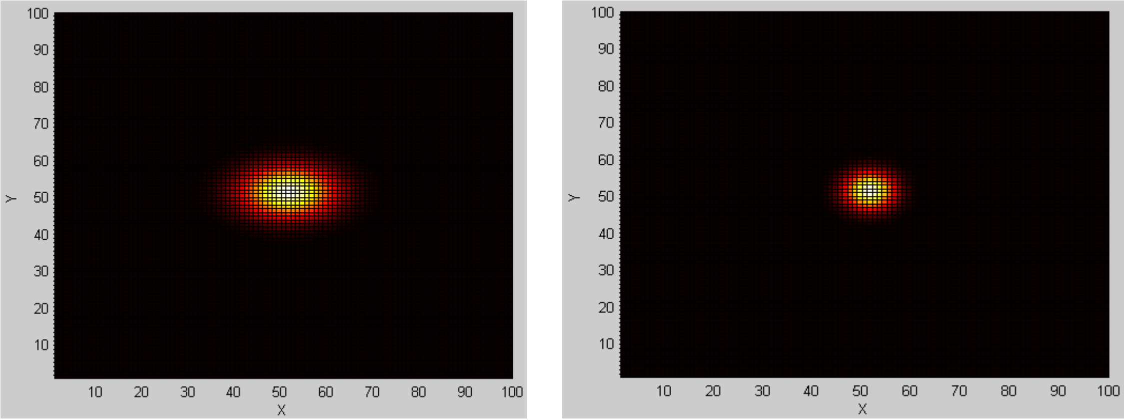

FIGURE 2.7: ROTATION VARIANT (LEFT) AND ROTATION INVARIANT (RIGHT) 2D GAUSSIAN WINDOWS
The graphs were plotted for values w_x*=3,* w_y*=5, k1=k2=1 and r=1.*

For most complex frequency domain implementations, Hartley transform is commonly used. Hartley transform assumes the even and odd parts of the signal/function to represent the real and imaginary frequencies respectively in the Fourier domain. Equation 2.4 shows Hartley transform definition for 2D continuous signal.

$$H\left(\omega_x,\omega_y\right)=\iint f(x,y)cas\left(2\pi x\omega_x+2\pi y\omega_y\right)\ \ dxdy \qquad (2.4)$$

where $cas(\theta)=\cos(\theta)+\sin(\theta)$

In this thesis the Hartley implementation of the rotation invariant 2D S transform was used for its computational advantages in that it doesn’t involve any comples arithematic.

CHAPTER 3

IMAGE ENHANCEMENT TECHNIQUES

3.1 INTRODUCTION

Due to external environmental factors and/or the image acquiring device, images could often be degraded. These images need enhancements for further specific use. Image enhancement is an essential field where visual appearance of an image is the main factor. Image enhancement is a process by which the output image is better suited for a specific task than the input. Enhancement covers different aspects of image corrections such as image saturation, sharpness, denoising, tonal adjustment, tonal balance, and contrast correction/enhancement [26] [27] [29]. In this thesis, contrast correction/enhancement was applied to enhance the CT lung images.

Image enhancement can be broadly classified as spatial domain image enhancement and frequency domain image enhancement

Spatial domain image enhancement: spatial domain enhancement is intensity-based calculation and transformation. It increases the dynamic range or the contrast of an image [25]. The general form is given by:

$$g(x, y) = T[f(x, y)] \tag{3.1}$$

where, $f(x, y)$ is the image on which the enhancement is going to be done, T is the enhancement transformation function and $g(x, y)$ is the resulting enhanced image.

Frequency domain image enhancement: this is mostly a Fourier domain image enhancement technique where the image data is first converted or transformed into another domain (frequency domain) [9]. Most of the enhancements that take place in this domain are image filtering and denoising through simplified convolution (multiplication) [9]. As briefly mentioned in the previous chapter (known result from Fourier theory), what requires lot of computations and operations in the spatial domain (convolution), can be done with a simple multiplication in frequency domain [9].

There are several frequency and spatial domain image enhancement techniques that exist in various literatures. But in this chapter focus is given to spatial domain image enhancement techniques and some of them are discussed below.

3.2 HISTOGRAM EQUALIZATION

Histogram equalization is one of the common spatial domain image enhancement techniques [28]. It generally uses the image histogram to stretch (and/or compress) the image contrast [28]. Image histogram relates the image intensities with their probabilities of occurrence [9]. For an image that assumes L possible intensity values, the discrete form of the equalized histogram could be computed using the formula in Equation 3.2.

$$s_k = \frac{L-1}{MN} \sum_{j=0}^{k} n_{j,} \qquad k = 0, 1, 2, \dots, L-1 \tag{3.2}$$

where n_j is the number of pixels assuming intensity value j, MN is the total number of pixels, and s_k is the number of pixels assuming intensity value k after histogram equalization. For a typical 8-bit image, L = 256.

Image histogram equalization stretches the image contrast between the two threshold values of maximum and minimum intensity values [9]. From the formula above, it is obvious that the histogram equalization process depends on how frequent a certain intensity value exists in the image. Histogram equalization could be performed both globally and locally. A direct application of Equation 3.2 offers global histogram equalization. However, if the process has to respond to local changes (most images show such local variation) within the image, adaptive histogram equalization is a preferred method [9]. This is done by applying histogram equalization over a translating window which localizes the process in space. The window size has to be chosen depending on the specific application that the output image is required for.

3.3 POWER LAW TRANSFORMATION

Power law transformation (gamma-transformation) is defined as:

$$s = cr^{\gamma} \tag{3.3}$$

where c and γ are positive constants, r is the input pixel intensity and s is the transformed intensity. These two constants are required for the image enhancement, where γ controls the contrast and c is required for controlling the brightness of the image [9] [29]. Gamma correction could be classified as global or local [29]. In global gamma correction, only one value of gamma (γ) is used for the whole image [29]. Power law transformation functions with different gamma values are depicted in Figure 3.1 below ($c = 1$ is assumed). Application of global power law transformation to an image may create an over enhancement or under enhancement is some parts of the image [29]. As a result, it is logical to use different gamma (γ) values for different parts of the image for better enhancement. This depends on classifying an image or part of an image (usually neighborhood) to be low contrast or better contrast. There are different methods as to group an image or part of an image as good contrast or bad contrast.

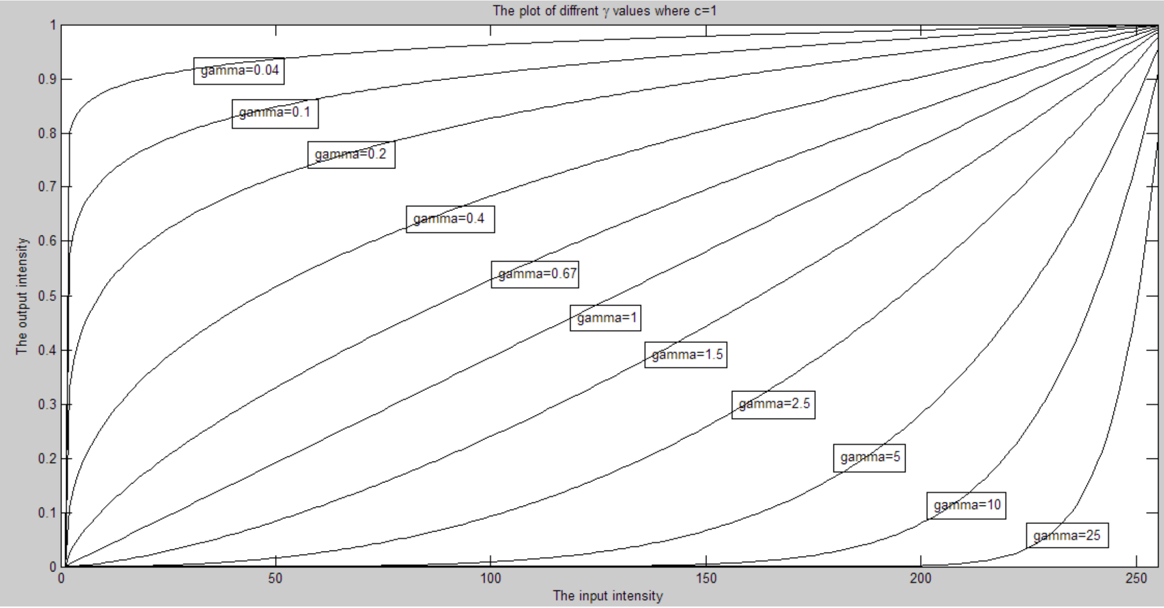

FIGURE 3.1: POWER LAW TRANSFORMATION FUNCTIONS FOR DIFFERENT GAMMA VALUES WITH C=1.

In a previous study, a windowed gamma correction with modified value of gamma was used [30]. The gamma is calculated as:

$$\gamma = (\frac{1}{2.2})^{(\frac{128-\mu(x,y)}{128})} \tag{3.4}$$

where, $\mu(x, y)$ is the local mean of the part of the image that needs to be corrected. The value 2.2 is an experimental value commonly used for gamma correction in most computer systems and standard displays [30]. Equation 3.4 was designed to do gamma correction on 8-bit images. As the value of γ >1, the contrast will be shrinking (assuming normalized image between 0 and 1). And if the value of γ <1, the contrast of the image will be stretched.

In some cases, the modified histogram might lose its statistical information after image histogram-based enhancement that preserves its brightness [31]. Thus, there has to be another histogram processing so as to preserve the statistical information as it was after the enhancement. As a result, weighting distribution was implemented in [31] to calculate the γ value. Weighting distribution function only slightly modifies the statistical information and reduces the generation of adverse effects [31]. The γ value is calculated for each intensity value as:

$$\gamma = 1 - cdf_w(l) \tag{3.5}$$

where $cdf_w(l)$ is weighting cumulative distribution function at intensity value l computed using Equations 3.6 and 3.7.

$$pdf_w(l) = pdf_{max}(\frac{(pdf(l) - pdf_{min})}{pdf_{max} - pdf_{min}})^{\alpha} \tag{3.6}$$

$$cdf_w(l) = \sum_{k=0}^{l} pdf_w(k) / \sum pdf_w \tag{3.7}$$

where $\sum pdf_w = \sum_{l=0}^{lmax} pdf_w(l)$, pdf is the probability density function at intensity l, $pdf_w(l)$ is the weighting distribution function at intensity l, pdf_{min} and pdf_{max} are the minimum and maximum values of $pdf(l)$ respectively while $\alpha = 2.2$ as in the previous case.

On another research, an image could be classified as low contrast when most of the pixel intensities of an image are clustered within a small range [29]. The criteria follows Chebyshev’s inequality which states that at least 75% values of any distribution will stay within 2σ around its mean on both sides. This leads to the criteria for an image to be grouped under low contrast image [29]. As for the brightness of an image, it is called bright image if its mean $\mu > 0.5$ (assuming the image is normalized between 0 and 1). Therefore, by preserving the brightness, the enhancement could be calculated using the procedure explained below.

First the image is categorized depending on contrast (low contrast and moderate-high contrast) and depending on the brightness (bright and dark). As a result, different formulas are used to calculate the values of $\gamma \; and \; c$. The output intensities for bright and dark images are given by Equations 3.8 and 3.9, respectively.

$$s = r^{\gamma} \tag{3.8}$$

$$s = \frac{r^{\gamma}}{r^{\gamma} + (1 - r^{\gamma}) \times \mu^{\gamma}} \tag{3.9}$$

where μ is the mean of the image.

For low and moderate-high contrast images, the formula for their respective gamma is calculated using Equations 3.10 and 3.11, respectively.

$$\gamma = -log_2 \sigma \tag{3.10}$$

$$\gamma = exp^{[\frac{1-(\mu+\sigma)}{2}]} \tag{3.11}$$

where, $\mu \; and \; \sigma$ are the mean and standard deviation of the image.

3.4 SUCCESSIVE MEAN QUANTIZATION TRANSFORM (SMQT)

The successive mean quantization transform (SMQT) was proposed by *Michael et al.* [27] on their paper published on IEEE journal in 2005. In SMQT, first the mean of the input dataset is calculated. Then depending on the calculated mean $\mu\big(I(x, y)\big)$ of the input image, image pixels will be grouped as pixels which have an intensity value greater than the mean and less than the mean. Image pixels with intensity values greater than the mean are given a value ***1*** and those with values less than the mean will be given value ***0.*** Then depending on the new values given to the image pixels, a binary coded image is formed. Then the image will be splitted into two (image contianing only greater values than the mean and images with lesser values than the mean). Each image is called MQU (mean quantization unit). The iteration is measured in terms of levels (we just completed level-1 by splitting the image into two using the total mean of the input image).

The next level continues accordingly by calculating the mean for each MQUs resulting from the first mean $\mu\big(I(x,y)\big)$. Then, the respective means for each denoted by $\mu 1\big(I(x,y)\big)$ and $\mu 2\big(I(x,y)\big)$ are used to split the two MQUs into 4 (each divided into two). This is the second level (level-2) resulting in 4-MQUs. Using this trend, it continues onto the next level. And at each level, there will be a binary coded image formed. Most of the time 8-level quantization is applied on images. The output of the SMQT is the combination of binary coded images formed at each level of the scheme. Thus, combination assumes the first binary coded image to be the most significant bit. As one goes from top to bottom, the binary coded images are having lower and lower significance. Having this order of significance they will be combined accordingly with their corresponding level (will be multiplied by 2^{l-1}; where l is the level of the SMQT) [26]. A schematic diagram showing the process of SMQT is shown in Figure 3.2.

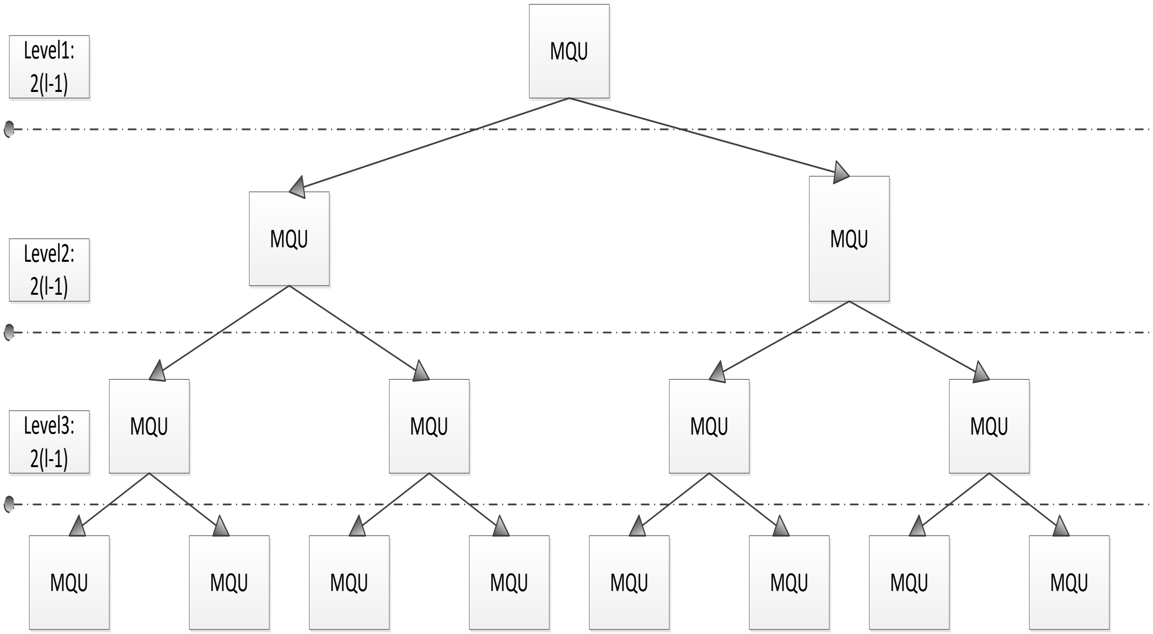

FIGURE 3.2: SUCCESSIVE MEAN QUANTIZATION TRANSFORM SCHEMATIC DIAGRAM.

The advantage of using SMQT is to have a quantized pixel intesnsity values that would be helpful in image segmentation and feature extraction. The quantized values help in calculating the threshold efficiently. An 8-level SMQT is implemented in this thesis for efficient enhancement of the CT lung images.

3.5 MARKER CONTROLLED WATERSHED TRANSFORM

The concept of watershed is based on visualizing an image in three dimensions. The two coordinates are the image coordinates and the other one is the intensity of pixels. In this interpretation there are three things to consider; points belonging to a regional minimum, points at which drop of water if placed at the location of any of those points would fall certainly to a single minimum and points at which water would be equally likely fall to more than one such minimum [9].

Assume a hole is punched in each regional minimum and the entire topography is flooded from the bottom. Assuming the water rise from the holes at uniform rate, as the water continues to rise, it will overflow from one catchement area into another. This effect is more pronouncd as the water continues to rise. This process continues until the maximum level of flooding is reached. The final dams are the outputs of the segmantation [9].

However, direct application of watershed usually encounters problem of oversegmantation due to noise and other local irregularities of the gradient. As a result, an approache based on marker is implemented to control the oversegmentation. A marker is a connnected component belonging to an image. There are internal markers associated with the objects and external markers associated with backgrounds [9]. This approach is later implemented in this thesis to segment only the lung parenchyma from the background identified on the CT images.

CHAPTER 4

PROPOSED LUNG CANCER DETECTION SCHEME BASED ON IMAGE PROCESSING USING LOCALIZED INTEGRAL TRANSFORM

4.1 INTRODUCTION

Lung cancer detection based on image processing is an active area of research and comes with several challenges. One of the difficulties is image feature extraction and segmentation. Differentiation between the lung and the rest of the thoracic parts and also between normal lung nodules and malignant nodules is a task that is not straight forward. Here in this chapter the series of steps and procedures that have been used for the proposed feature extraction and lung cancer segmentation scheme in this thesis are discussed.

There are a number of methods proposed for segmentation and feature extraction of digital images in general. Among many, transform-based image segmentation and feature extraction showed great promises in various applications. The whole idea is to transform the digital images from their original spatial domain to a transformed domain (commonly frequency domain) aiming for a more effective and efficient image processing. Once the image is transformed to the frequency domain for example, a way to manipulate its amplitude and phase information could be sought. In this regard, a number of integral transforms exist to choose from in various literatures. However, as explained in Chapter 2, those integral transforms that offer joint space and frequency information are more applicable particularly for medical images with frequency characteristics that show great spatial variation.

Among the different space localized integral transforms that exist in the literature, the rotation invariant S transform is favored in this thesis (see previous discussions). The rotation invariant S-transform has a better resolution of frequency as compared to the Gabor and it introduces less noise compared to the wavelet transform (this was explained in details in Chapter 2). In addition, the direct relation that exists between the S-transform and the natural Fourier transform makes is a better choice.

In this thesis, the spatial domain image enhancement was done on the images before applying the rotation invariant S-transfrom. The SMQT with adptive gamma correction was used for spatial image enhancement. The SMQT quantizes the intensity of the input image (this was explained in details in Chapter 3). Quantization of the intesnities does have an advantage in image segmentation and feature extraction. Then, the rotation invariant S transform is implemented on the spatially enhanced DICOM CT images of the lung acquired from the TCIA database. These were images taken from patients with some manifestation of lung cancers as confirmed by physicians, accompanied by the ground truth information used here as the gold standard. The images came with information about the cancer location (CT slice numbers and coordinates). Images taken from normal cases with no sign of cancer on their lungs (as seen on the CT scanner) are used as controls in this thesis work.

4.2 PROCEDURES

Four major steps were involved in the development of the cancer detection scheme in this thesis: image pre-processing, enhancement, feature extraction & segmentation and final image classification (see Figure 4.1). The four steps are explained subsequently below.

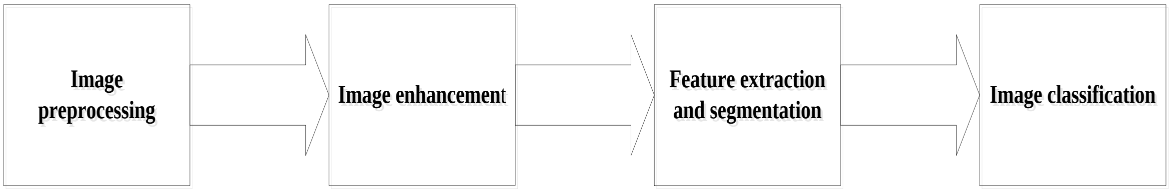

FIGURE 4.1: BLOCK DIAGRAM FOR THE WORKFLOW OF THE PROPOSED ALGORITHM.

4.2.1 IMAGE PRE-PROCESSING

The input to the system is a 16-bit DICOM image with a resolution of 512x512. Two basic techniques have been implemented during the pre-processing stage in a cascaded manner. These are the marker-controlled watershed transform and the area filter. The steps were preceded by image contrast stretching and normalization. The contrast stretching was done automatically through inbuilt matlab function *imadjust*. The raw DICOM CT images themselves provide a way to adjust the image intensity values between 0 to 1. Then the next step after normalization is the application of marker-controlled watershed transform and area filter. The techniques were applied to segment only the lung part of the CT images. Their output will further be used for segmentation and classification of normal and abnormal nodules. The binary image was used as an output from the marker-controlled watershed transform. A marker-controlled watershed implementation from *mathworks.com* was used for this purpose [34]. Before the watershed algorithm is applied, wiener filtering was utilized for a better image enhancement. In the watershed transform used in this thesis, the optimal threshold value was calculated using the Otsu algorithm (which assumes that the image contains two classes of pixels (foreground and background pixels), it then calculates the optimum threshold separating the two classes so that their combined intra-class variance is minimal) [34]. Then area filter was applied to the binary image output of the marker-controlled watershed transformed image. The area filter works based on the area of the segmented region of the binary image. The area of the lung perynchyma was calculated using the area filter assuming the lung region covers between ***1%*** and ***35%*** of the total pixels included in the image under consideration while the range was obtained experimentally.

After obtaining the result form the marker-controlled watershed and area filtering, the output binary image (showing only the lung region) will be fused with the original image. Then cropping the part of the original image by cropping the part of the fused image segmented by the marker-controlled watershed and area filtering algorithms will mean segmenting the lung part of the original image. After that, a 7x7 wiener filter was applied on the fused image aiming for further smoothing in which the result will be used later in the image feature extraction and segmentation stage. The cropping was done using the developed Graphical User Interface (GUI). A 3x3 wiener filter was further applied on the cropped image to avoid blurry edges and reduce noise level. All lung ROIs cropped using the above procedure are resized into dimension 120x150 in order to bring all to a common resolution before further processing. The resizing also has computational advantages by reducing the memory requirement of the 2D rotational invariant transform.

4.2.2 IMAGE ENHANCEMENT

At this stage, two techniques of spatial domain image enhancement were implemented on the pre-processed images: successive mean quantization transform (SMQT) and the adaptive gamma correction, both introduced in Chapter 3; the first enhancement was used to create a better contrast image. An 8-level SMQT was used in this regard. Here the cropped and resized image from the previous stage will be enhanced. Before using the SMQT, the depth of the image will be reduced from 16-bit to an 8-bit image. This will ensure fast computation and efficient memory consumption for the later stage. The SMQT delivers quantization to the pixel intensities of the input image. The quantization characterizes the image intensities with finite intensity values. This does ensure reduction of image information to only specific groups of pixel intesnities. This would help for characterizing the image by specific intensity feature which will later be used in image feature extraction and segmentation. However, the enhancement introduces some unnecessary intensity values. This is because of its dependency on the mean. If it has greater value than the mean, it will be categorized under some group. As a result, boundary valued intensities will have intensities that they don’t have. Therefore, another enhancement technique was required to rectify the error and enhance the images. For this adaptive gamma correction was implemented. Adaptive gamma correction would enhance the image contraction that could be resulted from the SMQT. This enhancement would correct contrast and brightnes as well (as explained in Chapter 3). The result of the processing was shown using an HSV (Hue, Saturation, Value) pseudo-coloring scheme. This was used because it is often very difficult to see slight intensity differences in gray scale-images and the HSV color converted CT images were visually more informative than the processed grayscale images due to the property of the HSV color space mapping to the human color vision. And it separates the intensity and the color. The HSV pseudo-coloring was done automatically using a Matlab built-in function. Whereas the SMQT and the adaptive gamma correction functions were coded from respective algorithms.

4.2.3 IMAGE FEATURE EXTRACTION AND SEGMENTATION

This stage is the most crucial part of the cancer detection procedure. It extracts useful image features and segments the image accordingly. The pre-processed and later spatially enhanced image has to be first transformed from the spatial domain to a joint space-frequency domain using the rotation invariant S transform. The rotation invariant S transform does have a 4D output. Hartley implementation of the rotation invariant S transform was used here. The real domain computation using the Hartley transform has a remarkable advantage in the efficiency of the computation as well as the memory requirement. After the frequency components are found, the amplitude spectrum was used to calculate the local power (the square of the amplitude). The amplitude spectrum was used instead of phase content of the transform since phase contains too much information which makes it difficult to extract useful features for specific application. Once the power is computed at each spatial position and for each spatial frequency in both x and y directions, the resultatnt power was computed as the sum of the powers at each spatial position using contributions from each spatial frequency components. The median, mean, kurtosis and skewness were also tested to compute the resultant power. However, the sum was found more informative. The resultant power then creates what we call in this thesis research the signature map which is the 2D image used for further image processing.

After the signature map is computed and normalized between 0 and 1, another step for image contrast enhancement was used. This is gamma correction. Through repetitive trials (from 20th power upto 10th root) on the image, the 10th root gamma correction was found to be adequate for all tested images. Image subtraction was later applied by computing the difference between the SMQT and adaptive gamma enhanced image and the gamma corrected image. Then the difference is added back to the image output of the pre-processing stage which is smoothed by the 7x7 wiener filter.

4.2.4 IMAGE CLASSIFICATION

This step was carried out by applying simple thresholding on the signature maps generated from the previous stage. Before thresholding, all signature maps were normalized between 0 and 1. As presented in the results section of this thesis, lung cancers appear green or cyan color on the generated signature maps and keeping those normalized signature map values between the interval [0.165, 0.2974] was able to completely segment the lung cancers from the rest of the background. This was done by applying a Gaussian thresholding.

4.3 TESTING AND VALIDATION

Tests have been done on the DICOM images acquired from the TCIA database to check the efficacy of the proposed system. Sensitivity, specificity and overall accuracies were calculated to quantify the performance of the proposed scheme where true positives, true negatives, false positives and false negatives had to be calculated using the available ground truth information as a gold standard. If we assume positive is for affected lung nodules and negative for healthy lung nodules, then true positive (TP) signifies the number of cases correctly identified as abnormal, false positive (FP) is the number of cases incorrectly identified as abnormal, true negative (TN) is the number of cases correctly identified as normal while false negative (FN) signifies the number of cases incorrectly identified as normal. Sensitivity, specificity and overall accuracy measures were performed based on the TP, FP, TN and FN values using formulas used in previous literatures [33].

In addition to the quantitative evaluation, the performance of the proposed method has also been compared qualitatively against other segmentation results already reported in different published journal articles.

4.4 MATERIALS USED

The entire lung cancer detection scheme has been implemented on a Matlab platform (Matlab 2013a). Codes and tutorials from *mathworks* have also been utilized. The proposed algorithm was developed on a Toshiba laptop (dual core @ 2GHz, 6 GB RAM, Microsoft Windows OS). The images acquired from the TCIA database were all grayscale, 16-bit, 512x512 resolution DICOM images acquired using a low dose CT imaging modality with helical mode scan option [32].

CHAPTER 5

RESULTS AND DISCUSSIONS

5.1 INTRODUCTION

Selected qualitative and quantitative results have been presented in this chapter to demonstrate the effectiveness of the proposed cancer detection scheme accompanied by discussions.

5.2 QUALITATIVE RESULTS

5.2.1 RESULTS FROM IMAGE PRE-PROCESSING

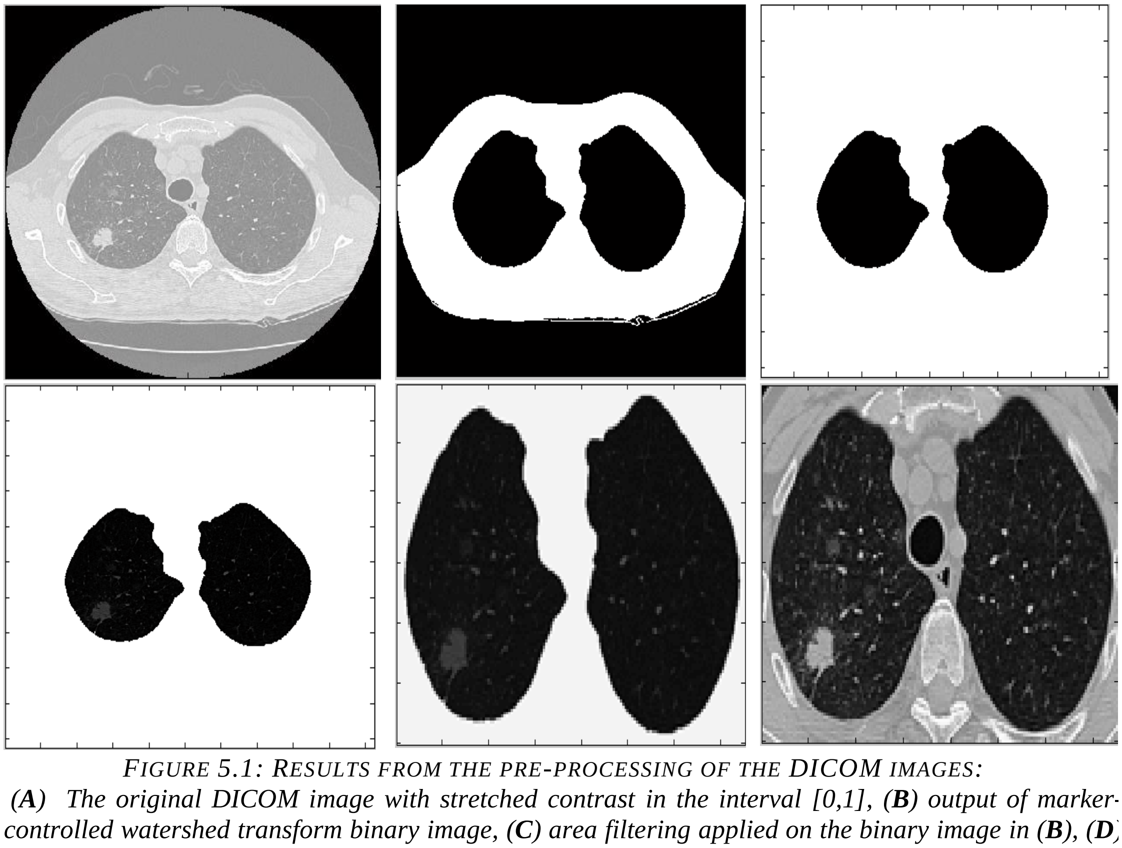

FIGURE 5.1: RESULTS FROM THE PRE-PROCESSING OF THE DICOM IMAGES:
*(**A**) The original DICOM image with stretched contrast in the interval [0,1], (**B**) output of marker-controlled watershed transform binary image, (**C**) area filtering applied on the binary image in (**B**), (**D**) fusing of original DICOM image and the binary image from (**C**), (**E**) and (**F**) are results after cropping is applied on the image in (**D**) and (**A**) respectively.*

A B C
D E F

Figure 5.1 presents a typical output during the pre-processing stage of the proposed algorithm. The original 16-bit depth, 512x512 resolution DICOM image was contrast stretched before the marker-controlled watershed algorithm and area filtering were applied. The threshold value used to generate the watershed processed image was derived using Otsu’s algorithm. The area filtering operation effectively segmented the lung parenchyma region. The final cropped image was able to retain the lung region with the surrounding tissues ready for further processing. The automated cropping is needed not only to select out the region of interest (the lung and its surrounding tissues) but also to make further processing computationally efficient. We notice that the 2D rotationally invariant S transform returns a 4D matrix output for a 2D gray scale discrete image as an input and hence requires a large memory to store. Cropping lessens the computational requirement considerably. One thing is obvious: it is possible to crop out the lung region with its surrounding tissue structures manually. But that is going to be too subjective and time consuming. The automation proposed here is both effective in cropping out the correct region of interest and at the same time very efficient as it needs only fraction of seconds to run. After that, the image will be filtered by 3x3 wiener filter to reduce blurring edges. Then the image will be resized to [120,150] to reduce memory requirement for the computation. The output of the cropping and resizing are shown on **E** and **F** sections of Figure 5.1. The image on **E** is the fused image which later be used in the feature extraction section after passing through smoothing by the 7x7 wiener filter.

5.2.2 RESULTS FROM IMAGE ENHANCEMENT

Figure 5.2 demonstrates the second stage results before feature extraction and segmentation: application of SMQT and gamma correction on the pre-processed images. What is noticeable is what happened to the histogram of the input images after the application of SMQT and gamma correction. The histograms show that the images have been very well quantized making the images ready for effective segmentation. Bunched up picks on the histogram plot depict different objects on the images.

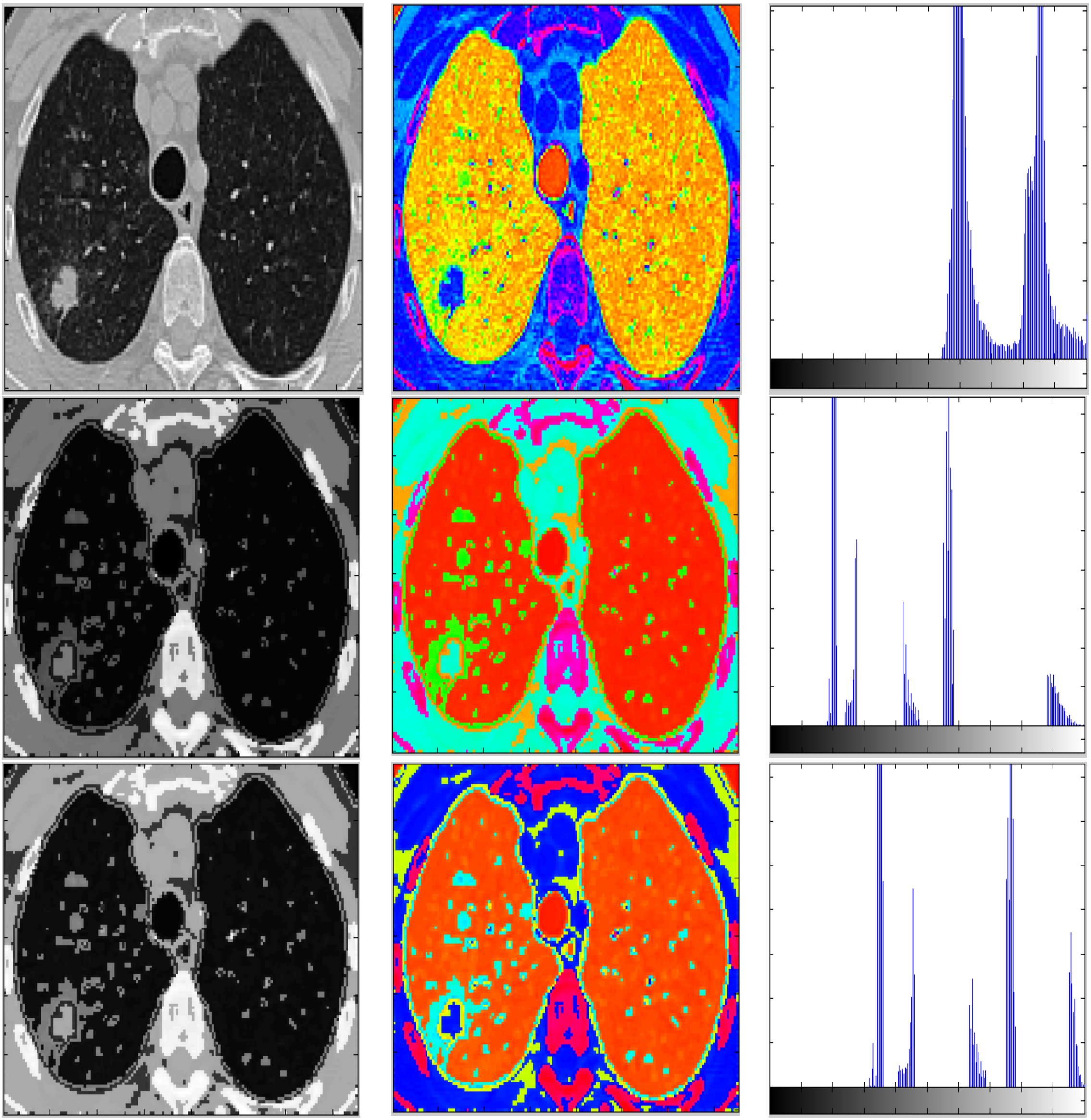

Figure 5.2: Results from the image enhancement of the pre-processed image: ***(A)*** *is the input image,* ***(D)*** *is the SMQT enhanced image and* ***(G)*** *is the gamma corrected image.* ***(B)****,* ***(E)*** *and* ***(H)*** *are the original, SMQT enhanced and the gamma corrected images plotted in the HSV color space respectively while* ***(C)****,* ***(F)*** *and* ***(I)*** *are the respective grayscale histograms.*

A B C
D E F
G H I

5.2.3 RESULTS FROM IMAGE FEATURE EXTRACTION AND SEGMENTATION

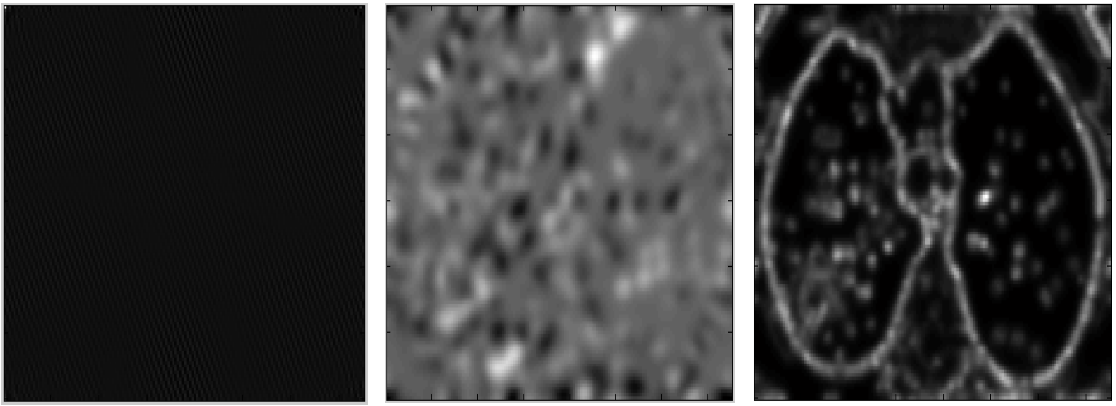

FIGURE 5.3: RESULTS OF THE ROTATION INVARIANT S-TRANSFORM:
*(**A**) is the sample frequency component of the S transform at pixel coordinates (25,90, :, :), (**B**) is the sample S transformed amplitude spectrum image at x-wavenumber ω_x=34 and y-wavenumber ω_y=34, (**C**) shows the power map computed by summing the resultant local powers (sums of squares of amplitudes) at each coordinate location.*

A B C

Figure 5.3 presents the local amplitude spectra (sliced from the 4D S transform at different frequency and spatial coordinate values) as well as the power map both generated after the application of the rotation invariant S transform on a typical CT lung image. Image **C** shows the output of calculating the power (as discussed in the methodology) and the sum.

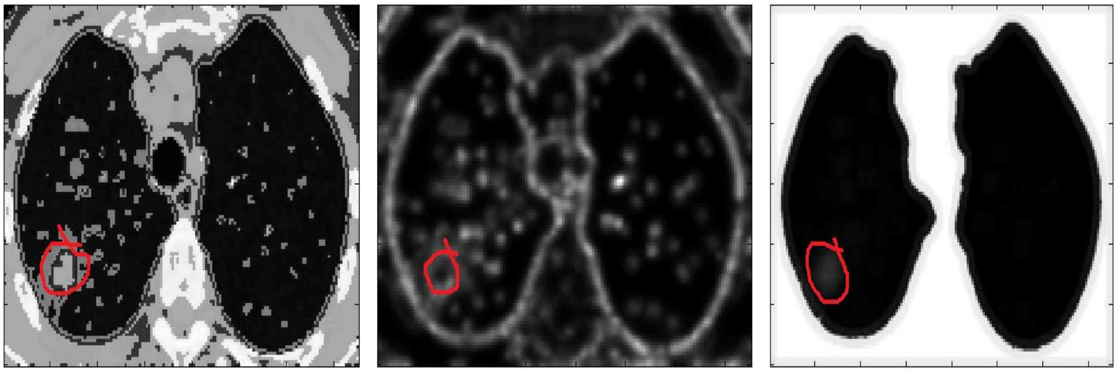

FIGURE 5.4: IMAGES USED FOR IMAGE FEATURE EXTRACTION:
*(**A**) is the input image after SMQT and gamma correction were applied, (**B**) is the power map computed from the rotation invariant S transform, and (**C**) is the wiener smoothed image after the marker-controlled watershed transform is applied. The red lines depict conformed lung tumor locations.*

A B C

Figure 5.4 demonstrates the outputs of the application of the SMQT and gamma correction, rotation invariant S transform (power map) and marker-controlled watershed transform (followed by wiener filtering) from, left to right respectively. We could concentrate on the SMQT and gamma corrected as well as on the power map images. If we look at the tumor area enclosed inside the red contour, we see that it is high intensity on the gamma corrected image while it appeared dark on the power map. If we subtract one from the other then, it will enhance the tumor region (abnormal lung nodules) significantly without that much affecting the surrounding tissues. Note that the power map is computed by taking the square of the local amplitudes. Other than taking the square, using different powers could affect the final subtracted image significantly. Different power values have been checked in this regard: 1/20, 1/9, 1/8, 1/7, 1/6, 1/5, 1/4, 1/3, 1/2, 1, 2, 3, 4, 5, 6, 7, 8, 9, 10. Generally power values which are less than 1 are found more informative. Figure 5.5 presents the image subtraction results between the SMQT enhanced plus gamma corrected image and that of different powers applied on the resultant magnitude of the S transform (powers 1, ½ and 1/10). Qualitative analysis done on most of the image samples considered showed that the 1/10 power offered the best visual results. In Figure 5.6 these subtracted images were re-plotted by a color indexing scheme in the HSV space. It is clear that subtracting the enhanced images from the 1/10 root of the resultant amplitude of the S transform resulted in the most compact lung tumor signatures.

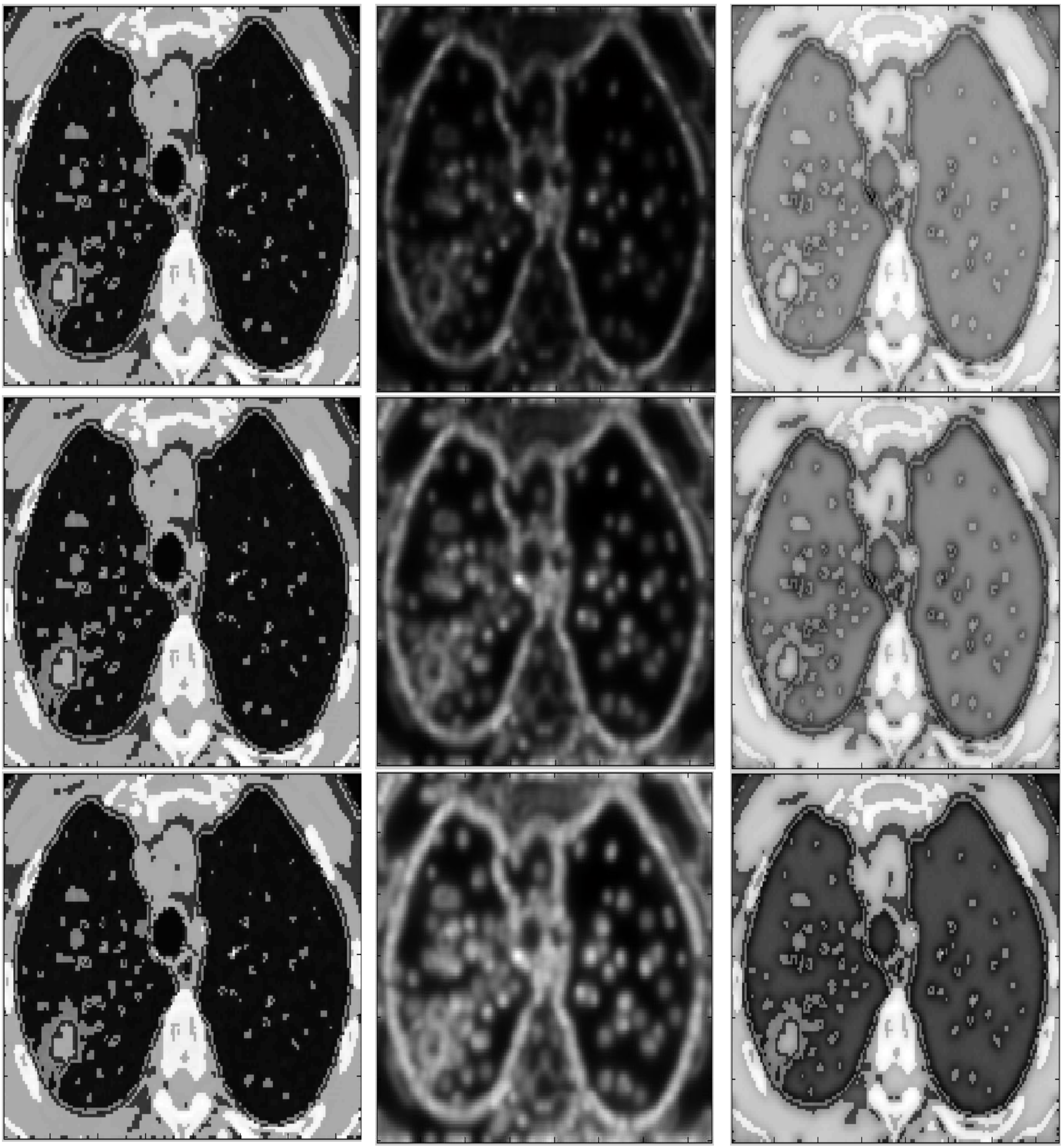

Figure 5.5: Images obtained by subtracting roots of the magnitude image from the enhanced image.

A, D, and G *are the SMQT + Gamma corrected images (with a tumor shown inside the red contour);* ***B, E, and H*** *are the magnitude images with roots 1, ½ and 1/10 respectively;* ***C, F and I*** *are the results of subtracting the magnitude images from the enhanced image.*

A B C
D E F
G H I

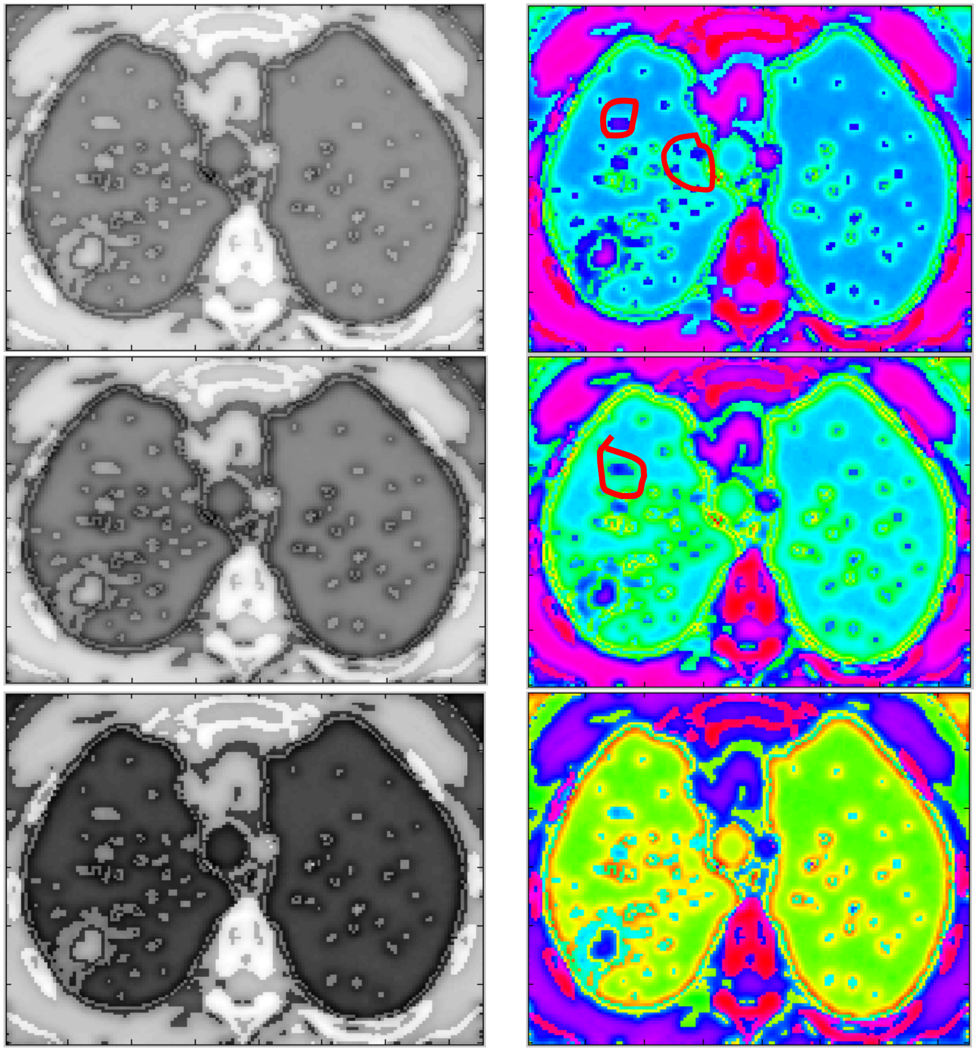

Figure 5.6: Images obtained by subtracting roots (1, ½ and 1/10 from top to bottom respectively) of the magnitude image from the enhanced image (first column) and the same using HSV color indexing (second column).

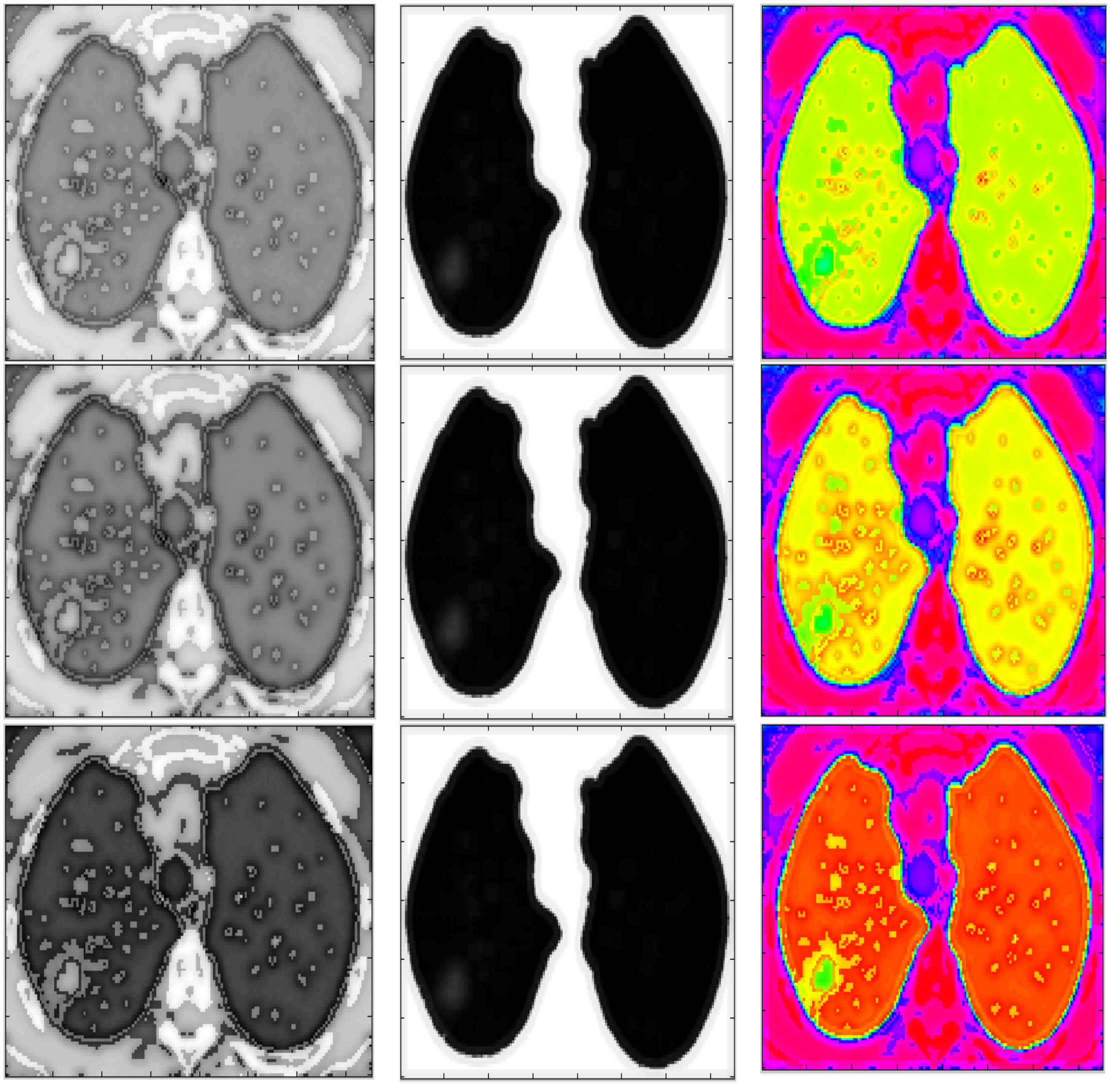

FIGURE 5.7: SUBTRACTED IMAGES OF THE ROOTS OF MAGNITUDES (1, ½ AND 1/10 RESPECTIVELY) FROM THE ENHANCED IMAGES (FIRST COLUMN), MARKER-CONTROLLED WATERSHED SMOOTHED IMAGES (SECOND COLUMN) AND THEIR RESPECTIVE SUM HSV COLOR INDEXING (THIRD COLUMN).

Figure 5.7 presents the final segmented images ready for further classification. It is clear from the figures that using the 1/10 root of the magnitude, subtracting the enhanced images from the magnitude images summed with the watershed smoothed images was able to display a clear lung cancer signature (green signature) on the HSV color indexing map. It was assumed that the information that is derived from these signatures could be used to accurately and automatically detect lung cancers making the classification procedure quite straight forward. In most of the image data considered in this thesis, the green signatures fairly match manual delineations performed clinically.

5.2.4 Result of image classification

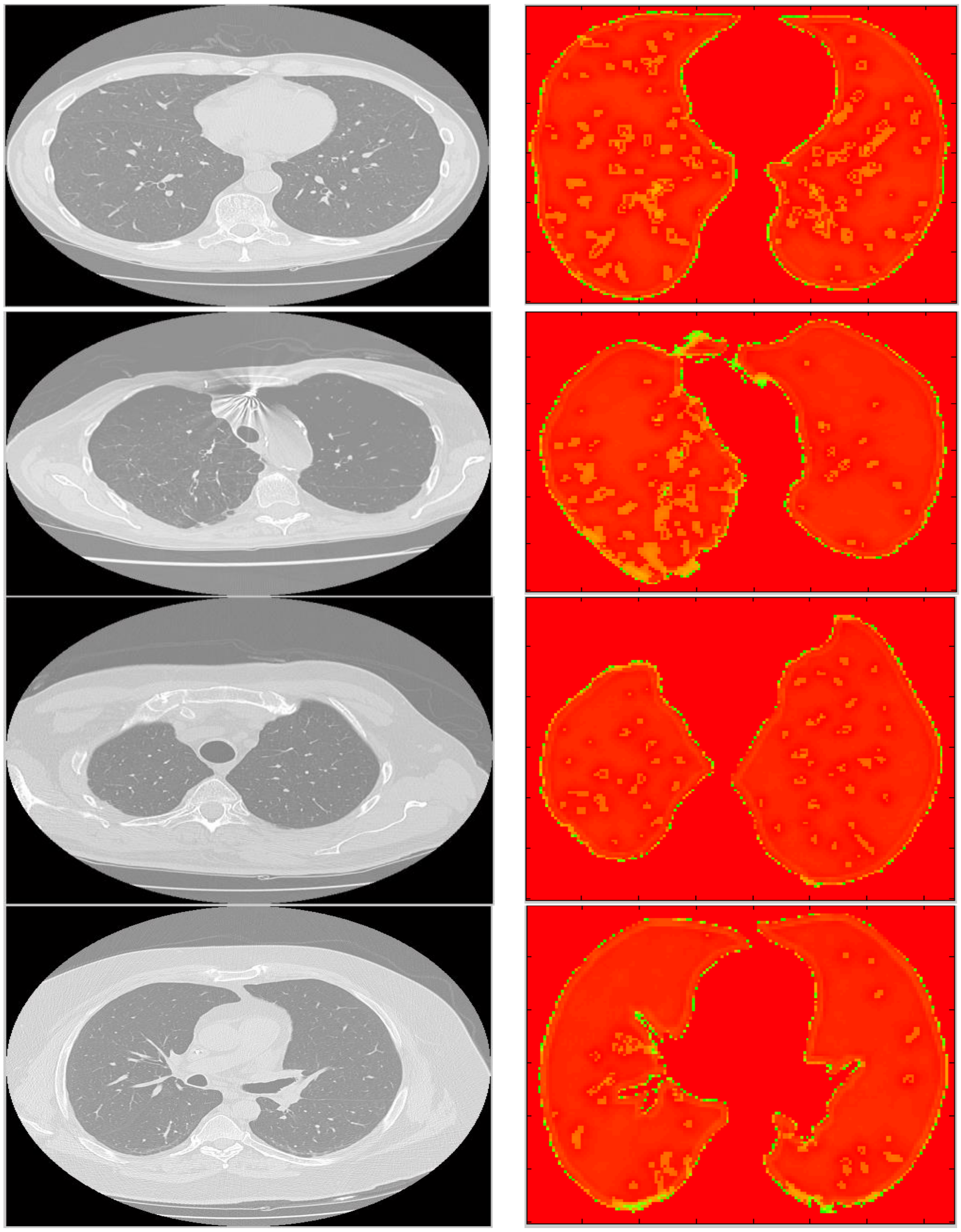

Figure 5.8: Normal images (controls) with no sign of lung tumors (first column) and classification results showing no green signatures (second column).

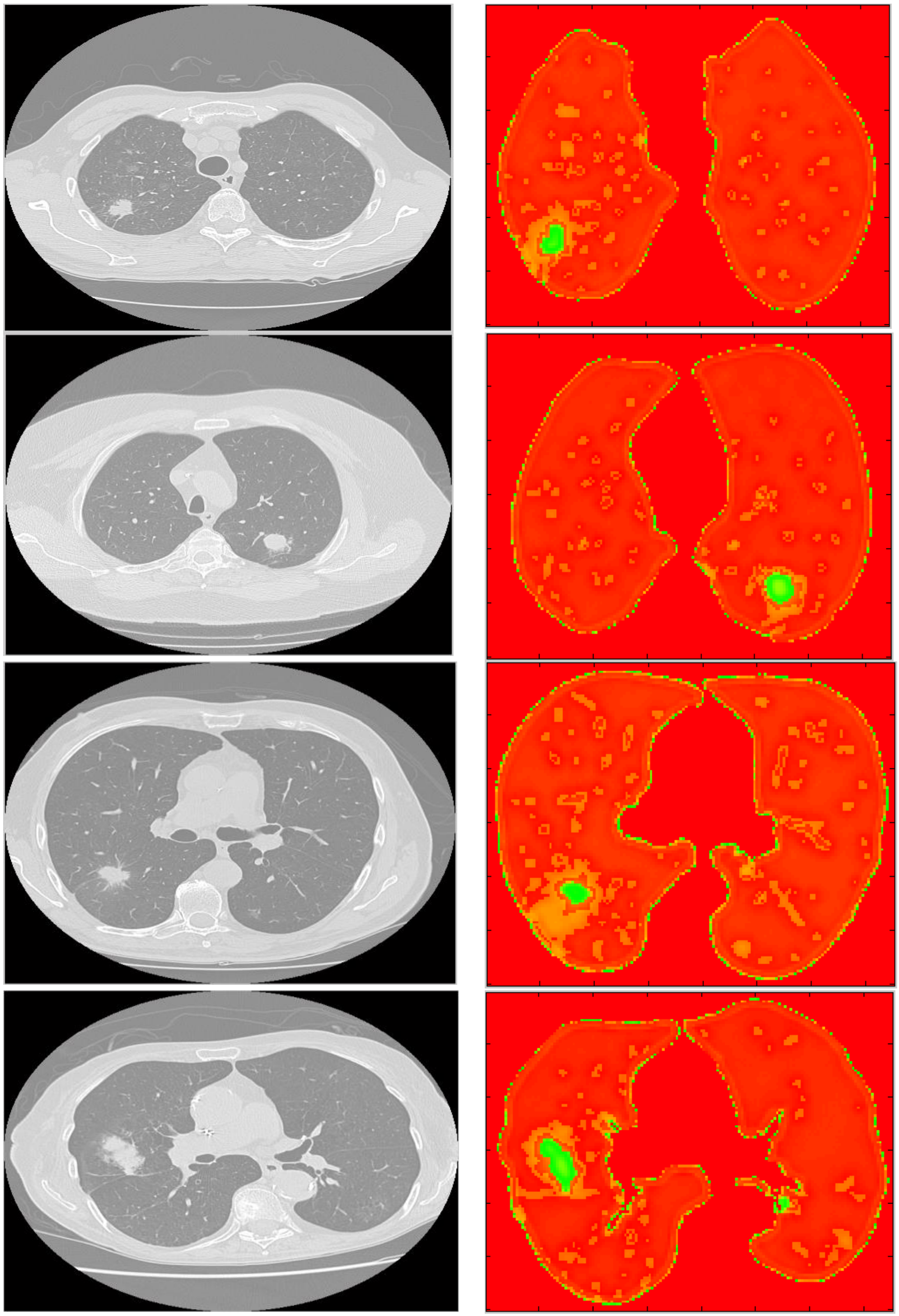

Figure 5.9: : Images showing some manifestations of lung tumors confirmed clnically (first column) and the respctive classified images where green signatures depict lung cancers (right column).

Figure 5.8 and Figure 5.9 present classification results for two groups of images: the first groups shown in Figure 5.8 composed of normal cases (control subjects) with no manifestation of lung cancers. Looking at the final signature maps in the HSV color space, no green signatures were seen confirming that the cases were indeed cancer free. The second group shown in Figure 5.9 contains lung images taken from lung cancer patients confirmed clinically. The location of the lung cancers varies from patient to patient as could be seen on the figures. Well compact cancer signatures (green signatures) are visible on the HSV color map showing the effectiveness of the proposed detection scheme. Similar results were found on most other images considered in this study.

5.2.5 RESULTS FROM LOW CONTRAST IMAGES

In order to check the robustness of the proposed cancer detection and classification algorithm, different images with variable degrees of difficulty were considered in this thesis work. Figure 5.10 presents visually low contrast lung images with some manifestation of cancers confirmed clinically. Not only the images were of low contrast but also the tumors were small in size pronouncing the degree of difficulty. Interestingly the proposed algorithm was able to detect all cancers accurately (green signatures). The low-resolution images were 8-bit images with size 140 x 220.

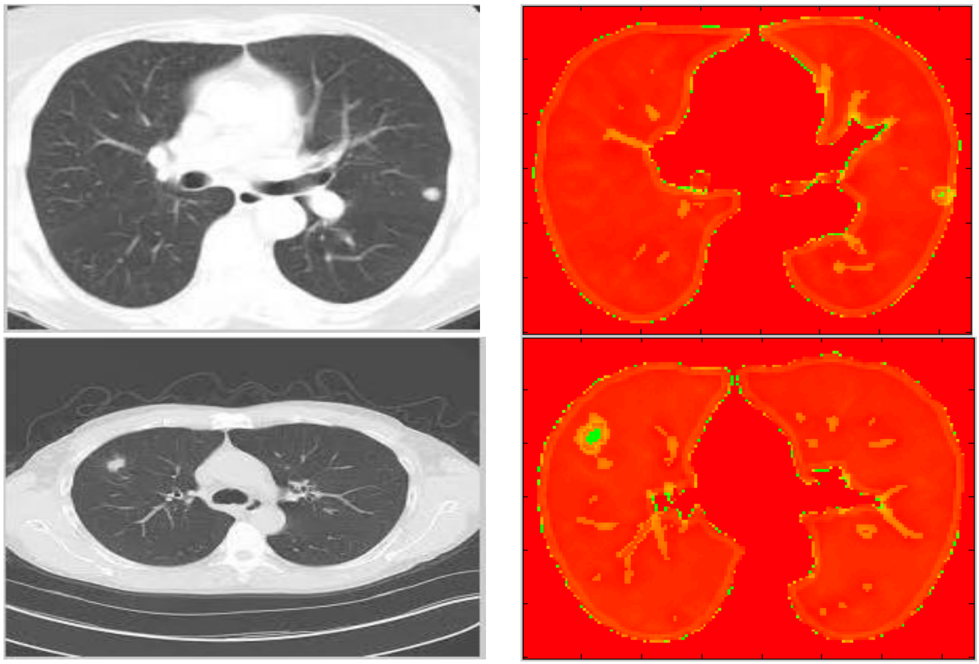

FIGURE 5.10: LOW RESOLUTION ABNORMAL IMAGES WITH SOME MANIFESTATION OF LUNG CANCERS (LEFT COLUMN) AND THE RESPECTIVE CLASSIFICATION RESULTS (RIGHT COLUMN).

5.3 QUANTITATIVE RESULTS

TABLE-1: TRUE POSITIVE, FALSE POSITIVE, TRUE NEGATIVE AND FALSE NEGATIVE VALUES COMPUTED USING THE PROPOSED ALGORITHM USING THE AVAILABLE GOLD STANDARD INFORMATION.

Status of lung	Total nodules	Abnormal nodules	Normal nodules	FP	FN	TP	TN
Abnormal	26	1	25	0	0	1	25
Normal	40	0	40	0	0	0	40
Abnormal	8	1	7	1	0	1	6
Normal	14	0	14	2	0	0	12
Abnormal	26	1	25	0	0	1	25
Normal	20	0	20	0	0	0	20
Abnormal	27	1	26	0	0	1	26
Normal	25	0	25	0	0	0	25
Abnormal	20	1	19	0	0	1	19
Normal	25	0	25	1	0	0	24
Abnormal	30	1	29	0	0	1	29
Normal	26	0	26	0	0	0	26
Abnormal	26	1	25	2	0	1	23
Normal	30	0	30	4	0	0	26
Abnormal	17	1	16	0	1	0	16
Abnormal	20	1	19	0	1	0	19
Normal	10	0	10	0	0	0	10
Abnormal	4	1	3	0	0	1	3
Abnormal	20	2	18	0	1	1	18
Abnormal	17	1	16	0	0	1	16
Abnormal	12	1	11	0	0	1	11
Abnormal	25	2	23	0	0	2	23
Abnormal	25	1	24	2	0	1	22
Abnormal	19	1	18	2	0	1	16
Total nodules	512	18	494	14	3	15	480

Table 1 presents the true positive, false positive, true negative and false negative values computed by comparing the classification outputs of the proposed algorithm with the available ground truth information used in this study as a gold standard. The first 17 cases were normal and abnormal nodules taken from sample (random sampling) images acquired from the TCIA database while the rest are only normal nodules taken from snapshots of lung images used in previously published journal artciles. Accordingly sensitivity, specificity and overall accuracy values were computed as follows:

$$Accuracy = (\frac{TP+TN}{TP+FN+FP+TN}) \times 100$$

$$= \left(\frac{495}{512}\right) \times 100 = 96.68\%$$

$$Sensitivity = (\frac{TP}{TP+FN}) \times 100$$

$$= \left(\frac{15}{15+3}\right) \times 100 = 83.33\%$$

$$Specificity\ = (\frac{TN}{TN+FP}) \times 100$$

$$= \left(\frac{480}{480+14}\right) \times 100 = 97.1\%$$

The algorithm achieved a commendable specificity of 97.1%, sensitivity of 83.3% and overall accuracy of 96.68%. Many image samples with different degrees of difficulty have been considered during the computation of the classification accuracy and the results obtained clearly showed the great promises of the proposed algorithm.

The computational efficiency of the proposed algorithm has also been checked. Accordingly, it takes an average of 65.41 seconds for the entire algorithm to run (on a Matlab platform) starting from loading a given CT lung image until a final classification result is found. The time of computation is reasonably low compared to other more complicated methods reported in the literature.

CHAPTER 6

CONCLUSION AND RECOMMENDATION

6.1 CONCLUSION

The main objective of the thesis was to design a robust, simple and accurate computer aided detection method for lung cancers based on low dose CT images of the lung. A number of literatures were reviewed to understand implementations of existing lung image analysis techniques. The application of integral transforms was given more emphasis. It was found out that the 2D rotation invariant S transform was a more convenient tool which could be used for effective and efficient analysis of the lung CT images.

Promising results were obtained using the application of the S transform based lung cancer detection and segmentation tool developed in this thesis. Enough image data have been tested to check the performance of the proposed algorithm. The image data was composed of subjects with different degrees of difficulties to check the robustness of the algorithm. In all cases the algorithm performed very well with an overall accuracy of about 96%.

6.2 RECOMMENDATIONS AND FUTURE WORKS

Though the performance of the proposed algorithm is found to be promising, however, there are still rooms for improvement. Enhancing the sensitivity is one major issue. The clinical validation of the work is also missing in the current study. This might require testing to be carried out on more number of data, inclusion of an observer study as well as piloting. These and similar other issues need much further investigations. Development of a complete CADx system is also worth trying. It takes about 65 seconds for the entire algorithm to run until a final classification result is generated on a Matlab platform. At this stage of the research, no rigorous effort was exerted on optimizing the program used to implement the algorithm. If optimized, the algorithm could run very fast and be applicable in real time processing which requires more work to be carried out.

BIBLIOGRAPHY

[1] S.Shaik Parveen, C.Kavitha. “A Review on Computer Aided Detection and Diagnosis of Lung Cancer Nodule.” *International Journal of Computers & Technology*, vol.3, pp. 393-400, Dec. 2012.

[2] A. del Ciello, A. R. Larici, P. Franchi, M. Ciresa, A. Contegiacomo, L. Bonomo. (2012, June). “Missed Lung Cancer at Chest Radiography: Prevalence and Radiographic Lesion Characteristics.” *European Society of Thoracic Imaging.* [Online]. pp. 1-11, Available: http://dx.doi.org/10.1594/esti2012/E-0107 [Oct., 23, 2016].

[3] D.L.de G. Hernández. (2015, Aug.). “The role of PET/CT imaging in lung cancer”. *Journal of Cancer Therapy*. [Online]. 6, pp. 690-700, Available: http://dx.doi.org/10.4236/jct.2015.68076 [Dec., 16, 2016].

[4] Winfield Boerckel, “Type and staging of lung cancer.” [Online], Available: http://www.lungcancer.org/find_information/publications/163-lung_cancer_101/ 268-types_and_staging, Nov. 2016 [2016, Dec.]

[5] S. C. van’t Westeinde and R.J. van Klaveren. “Screening and Early Detection of Lung Cancer.” *The Cancer Journal*, vol.17, pp. 3-10, Jan. 2011.

[6] A. Christe, L. Leidolt, A. Huber, P. Steiger1, Z. Szucs-Farkas, J. ROOS, J. Heverhagen, L. Ebner; Bern/CH, Bern, De/CH, Biel/ Bienne/CH, Winterthur/CH. (2013, Jan.). “Lung cancer screening: evaluation of radiologists and different computer assisted detection software (CAD) as first and second readers for lung nodule detection at different CT dose levels.” *European Society of Thoracic Imaging*, [Online]. pp. 1-11, Available: http://dx.doi.org/10.1594/ecr2013/C-2614, [Dec., 16, 2016].

[7] M. Firmino, A. H. Morais, R. M. Mendoça, M. R. Dantas, H.R. Hekis and R. Valentim. (2014, Jan.). “Computer-aided detection system for lung cancer in computed tomography scans.” *Review and Future Prospects Biomedical Engineering online.* [Online]. 13(41), pp. 1-16, Available:http://www.biomedical-engineering-online.com/content/13/1/41 [Dec., 24, 2016].

[8] K.N. Jeon, J. M. Goo, C.H. Lee, Y. Lee, J.Y. Choo, N.K. Lee, M. Shim, I.S. Lee, K.G. Kim, D.S. Gierada, and K.T. Bae. “Computer-aided Nodule Detection and Volumetric

to Reduce Variability between Radiologists in the Interpretation of Lung Nodules at Low-dose Screening CT." *Investigative Radiology,* vol.47, pp. 457-461, Aug. 2014.

[9] Rafael C. Gonzalez and Richard E. Woods. *Digital Image Processing*. Pearson Education International, 2002, pp. 132-145, pp. 222-263, pp. 483-527, pp. 791-801.

[10] Rene Carmona, Wen-Liang Hwang and Bruno Torresani. *Practical Time Frequency Analysis*. Academic Press, 1998, pp. 25-55.

[11] Ronald N. Bracewell. *Fast Fourier Transform and Its Applications*. McGraw Hill, 2000, pp. 293-295.

[12] M.V. Ajil and S. Sreeram. "Lung Cancer Detection from CT Image using Image Processing Techniques." *International Journal of Advance Research in Computer Science and Management Studies*, vol.3, pp. 249-254, May, 2015.

[13] Tudor Barbu. "Gabor Filter-based Face Recognition Technique". *Proceedings of Romanian Academy*, vol.11, pp. 277-283, March, 2010.

[14] Robi Polikar. Tutorial lecture, Topic: "The Wavelet Tutorial." 136 Rowan hall, Department of electrical and computer engineering, Rowan University, Glassboro, June 5,1996.

[15] L. Gabralla, H. Mahersia and M. Zaroug.. "Denoising CT Images using Wavelet Transform." *International Journal of Advanced Computer Science and Applications*, vol.6, pp. 125-129, May. 2015.

[16] I. Khalifa, A. Youssif and H. Youssry. "MRI Brain Image Segmentation based on Wavelet and FCM Algorithm." *International Journal of Computer Applications*, vol.47, pp. 32-39, May. 2012.

[17] R. G. Stockwell, L. Mansinha, and R. P. Lowe. "Localization of the Complex Spectrum: The *S* Transform." *IEEE Transactions on Signal Processing*, vol. 44, pp. 998-1001, April, 1996.

[18] D. Assefa, L. Mansinha, K. F. Tiampo, H. Rasmussen, K. Abdella. "The Trinion Fourier Transform of Color Images." *Signal Processing,* vol. 91, pp. 1887–1900, Feb. 2011.

[19] D. Assefa, L. Mansinha, K. F. Tiampo, H. Rasmussen, K. Abdella. "Local Quaternion Fourier Transform and Color Image Texture Analysis." *Signal Processing,* vol. 90, pp. 1825–1835, Feb. 2010.

[20] Gurpreet Kaur and Rajdavinder Singh. “Image Enhancement and its Techniques A-review.” *International Journal of Computer Trends and Technology*, vol.12, pp. 148-151, Jan. 2014.

[21] Leelavathi H. P. and Ram Manohar Nisarg. “Comparative study of Frequency Vs Spatial Domain for Multisensory Image Fusion.” *International Journal of Innovative Research, Engineering and Technology*, vol. 3, pp. 14242-14249, Jul. 2014.

[22] Sami Abdullah, Mohsen Salh and Haidi Ibrahim. “Mathematical Equation for Homomorphic Filtering in Frequency Domain: A literature survey.” International conference on information and knowledge management, vol. 45, pp. 74-77, 2012.

[23] Robert X. Gao and Ruquiang Yan. *Wavelet-Theory and Application for Manufacturing*, Springer, 2011, pp. 21-25.

[24] M. Sifuzzaman, M. R. Islam and M. Z. Ali. “Applications of Wavelet Transform and its Advantages Compared to Fourier Transform.” *Journal of Physical Science*, vol.13, pp. 212-134, Oct. 2009.

[25] David I. Houlding. “Pyramid Coding for Image and Video Compression.” MSc., Simon Fraser University, South Africa, 1994.

[26] Ma Jing, Zou Chengmeng, Jin Xiaolong. “An Improved Image Enhancement Algorithm.” *Wuhan University Journal of Natural Science*, vol.22, pp. 85-92, Feb. 2017.

[27] Mikael Nilsson, Mathias Dahl and Ingvar Claesson. “The Successive Mean Quantization Transform.” *IEEE International Conference on Acoustic, Speech and Signal Processing*, vol.4, pp. 429-432. 2005.

[28] Raman Maini and Himanshu Aggarwal. “A Comprhenssive Review of Image Enhancement Techniques.” *Journal of Computing*, vol.2, pp. 8-13, March. 2010.

[29] Shanto Rahman, Md Mustafijur Rahman, M. Abdullah-Al-Wadud, Golam Dastegri Al-Quaderi and Mohammad Shoyaib. ”An Adaptive Gamma Correction for Image Enhancement.” *EURASIP Journal of Image and Video Processing*, vol.35, 2016.

[30] Chun-Min Tsai. “Adaptive Local Power Law Transformation for Color Image Enhancement.” *Applied Mathematics and Information Science*, vol.7, pp. 2019-2026, Sep. 2013.

[31] Shih-Chia Huang, Fan-Chieh Chang and Yi-Sheng Chiu. “Efficient Contrast Enhancement using Adaptive Gamma Correction with Weighting Distribution.” *IEEE Transaction on Image Processing*, vol.22, pp. 1032-1041, March. 2013.

[32] Zhao, Binsheng, Schwartz, Lawrence H, & Kris, Mark G. “Data From RIDER_Lung CT”. *The Cancer Imaging Archive*. [Online], Available: http://doi.org/10.7937/K9/TCIA.2015.U1X8A5NR

[33] Alireza Baratloo, Mostafa Hosseini, Ahmed Negida, Gahad El Ashal. “Simple Definition and Calculation of Accuracy, Sensitivity and Specificity.” *Emergency,* vol.3, pp. 48-49, Feb. 2015.

[34] “Marker-controlled watershed segmentation Matlab implementation.” [Online], Avialable:http://www.mathworks.com/help/images/examples/marker-controlled-watershed-segmentation.html?requestedDomain==ve, Nov. 2016 [2016, Dec.]

APPENDICES

The Matlab Code

```
% Image read and contrast stretch for display
im = dicominfo('C:\””\””\””\””\””\RIDER-1500037140\000129.dcm');
im2 = dicomread(im);
im2 = imadjust (im2, stretchlim(im2), [0 1]);

% Image pre-processing, cropping and resizing
% application of marker-controlled watershed transform and area
% filter
im2 = im2double(im2);
[im3 bw] = watershed1(im2);
[im2 rect] = imcrop(im2);
im3 = imcrop(im3, (rect));
im2 = imresize(im2, [120 150]);
im3 = imresize(im3, [120 150]);

% Image smoothing through wiener filtering
im2 = wiener2(im2, [3 3]);

% Image enhancement by successive quantization transform and
% adaptive gamma
im2 = sqmt1(uint8(im2));

% The rotation invariant S-transform code from Dr. Dawit et al
rstd = PH_rot_inv1(im2);

% Calculation of power from the transformed image
for i = 1 : xr
    for j = 1 : xc
                m = ((rstd(i, j, :, :)).^2);
                I1(i,j) = (sum(sum(m)));
    end
end

% Normalizing the output data from the transform
I1 = I1 / max(max(I1));

% Smoothing the value from the marker-controlled watershed
transform
      im3 = wiener2(im3, [7 7]);

% Combinations of the three data for feature extraction and
% thresholding
dm = imsubtract(im2, real(power(I1,10))) + im3;
x3 = threshimage(x / max(max(x)));
```